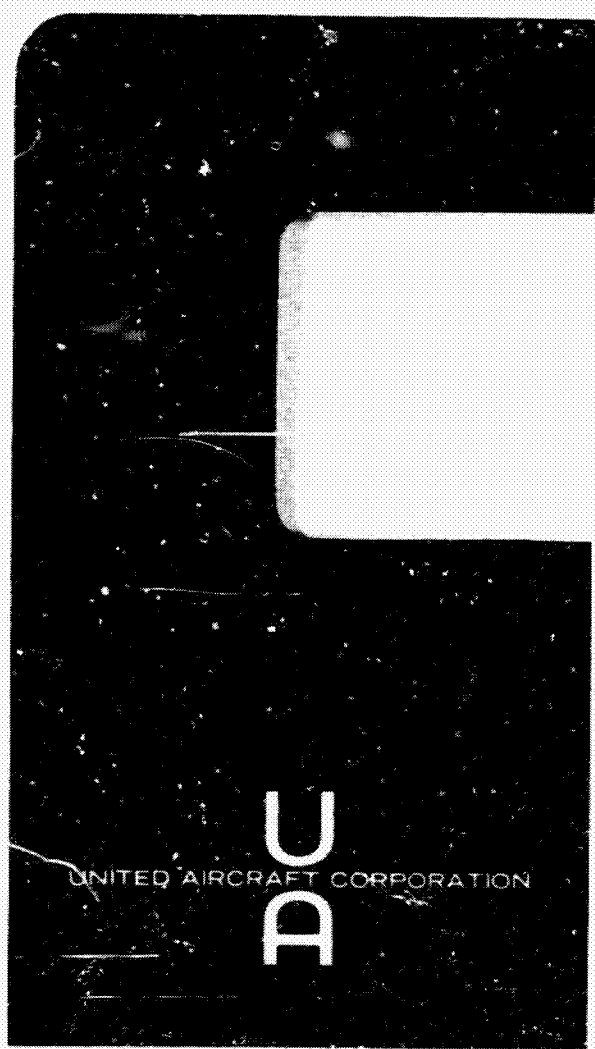
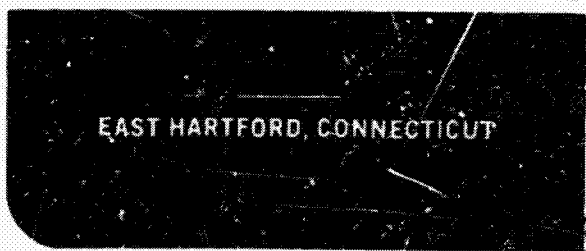


N.F.

N70-12234



United Aircraft Research Laboratories



N70-12234	(THRU)
CR-707045	(CODE)
(NASA CR OR TMX OR AD NUMBER)	(CATEGORY)



United Aircraft Research Laboratories



H-910093-44

Investigation of Gaseous Nuclear
Rocket Technology

Quarterly Progress Report No. 23
March 16, 1969 through June 15, 1969
Contract NASw-847

EDITED BY: G. H. McLafferty
G. H. McLafferty

DATE June 30, 1969

NO. OF PAGES 55

COPY NO. 13

Report H-910093-44

Investigation of Gaseous Nuclear Rocket Technology

Quarterly Progress Report No. 23 - March 16, 1969 through June 15, 1969

Contract NASw-847

SUMMARY

The investigation of gaseous nuclear rocket technology under Contract NASw-847 covers work in the following technical areas: experimental investigations of vortex flow, primarily in an r-f heated vortex, to obtain information for application to a nuclear light bulb reactor; studies of coaxial flows; studies of the radiant heat transfer spectrum emitted from the fuel region of a nuclear light bulb reactor; studies of radiation effects on the transmission characteristics of transparent materials mounted in the Langley Dynamitron electron accelerator and in a conventional continuous reactor; and studies of the characteristics of full-scale engines and of models which might be tested in the Pewee test reactor. During the current report period, the maximum power deposited in a gas discharge by the r-f heater was increased from 130 to 215 kw. At this higher power level: the power radiated through the peripheral wall was 156 kw; the corresponding radiating flux based on the discharge surface area was 36.7 kw/in.²; and the corresponding equivalent black-body radiating temperature was 10,200 R. Preliminary tests of models employing 0.01-in.-wall-thickness tubes were conducted, and models having 0.005-in.-wall-thickness tubes have been fabricated. In the coaxial flow program, tests were conducted with several different inlet configurations. Results of a series of tests performed at the Langley Dynamitron electron accelerator indicated that the steady-state absorption coefficient at the center of the 0.215-micron absorption band in fused silicon increased with either an increase in electron flux or a decrease in specimen temperature. Preliminary results were obtained from a portion of the program designed to calculate engine characteristics during transient operation.

The investigation described herein is being carried out under Contract NASw-847 with the National Aeronautics and Space Administration through the Space Nuclear Propulsion Office.

H-910093-44

FLUID MECHANICS OF NUCLEAR LIGHT BULB REACTOR
(J. S. Kendall, et al)

During this report period, significant results were obtained in all program areas. In the r-f light source research programs, the FY 69 goal of 150 kw of power radiated from the light source has been attained, and the maximum power deposited in a gas discharge has been increased to 215 kw. For this test the energy flux through the discharge periphery was 36.7 kw/in.^2 , which corresponds to an equivalent black-body radiating temperature of 10,200 R. Development of transparent-wall models and components was continued. A transparent-wall model with 0.005-in.-wall-thickness coolant tubes has been fabricated. Gas discharge tests employing this model will be conducted early in the next report period. Gas discharge tests employing a 0.010-in.-wall-thickness model were conducted in the 1.2-megw r-f induction heater. These tests are described in a following section. In the area of propellant heating research, the first series of demonstration tests were conducted in the d-c arc facility. In the area of vortex fluid mechanics research, the experimental investigation of seeded plasmas in the 80-kw r-f heater was continued and additional isothermal two-component vortex containment tests were conducted in the high Reynolds number facility. A discussion of the current status of the entire Fluid Mechanics Research Program is presented in the following section.

R-F Light Source Research
(W. C. Roman)

Test Configuration

For most tests the test geometry and diagnostic equipment employed was identical to that described in Quarterly Progress Report No. 22. However, for a few tests, two changes were made. First, swirl injectors were employed on both end walls. This produced a more symmetric injection configuration and permitted stable operation at higher power and pressure levels than had been previously achieved. Secondly, the ID of the swirl injection tubes was reduced from 0.10 to 0.067 in. The test configuration was pressure tested to greater than 20 atm prior to conducting gas discharge tests.

Discussion of Principal Results

The major objectives of the gas discharge tests conducted during this report period were to increase the total steady-state r-f power deposited in the discharge and to increase the discharge pressure above those levels which have been previously obtained. Significant increases were obtained in both areas; specifically, a 65 percent increase in the total power deposited in the plasma and an 84 percent increase in the discharge pressure over those previously reported. The maximum power deposited in the plasma in any test was 215 kw.

For this test the discharge pressure was 8.5 atm and the argon weight flow was 0.030 lb/sec. Additional results and a summary of the energy losses in various components of the system are presented in Table I. An average temperature of 20,500 R within the plasma was determined from the measured plasma volume, the measured total radiation, and Ref. 1. The measured radiant energy flux from the periphery of the discharge corresponds to an equivalent black-body radiating temperature of 10,200 R.

Results of all the most recent gas discharge tests are presented in Figs. 1 to 4. The argon weight flow rates were varied between 0.010 and 0.041 lb/sec and the discharge diameter varied from 0.62 to 0.95 in. (see Fig. 1). The optical scanning system (described in Quarterly Progress Report No. 22) was used to determine the plasma diameter. The diameter was measured at the axial midplane of the discharge. Photographs of the discharge were taken from various angles to aid in estimating the plasma shape.

In the tests at the highest power levels, $Q_T \geq 175$, the discharge diameter was intentionally allowed to increase slightly because of a limitation in the r-f induction heater (specifically, existing cooling capability of the vacuum capacitors within the resonator limits the peak r-f current for steady-state operation to approximately 1500 amp). This increase in plasma diameter was achieved by decreasing the argon weight flow and discharge pressure.

The variation of radiant energy flux with total discharge power is presented in Fig. 2. The radiant energy flux, ϕ_R , is:

$$\phi_R = (Q_W + Q_R - Q_C)/A_S \quad (1)$$

where Q_W is equal to the power deposited in the peripheral-wall cooling water-dye mixture, Q_R is the power measured by the radiometer located outside of the test chamber, Q_C is the estimated power conducted through the fused silica tube which forms the peripheral wall of the vortex chamber, and A_S is the surface area of the discharge. For the tests reported herein, Q_C was not directly measured. Estimates of the magnitude of Q_C were made by calculating the heat which could be conducted through the fused silica wall adjacent to the plasma for a wall surface temperature of 1800 F. Experience has indicated that rapid cooling of fused silica from temperatures in excess of 1800 F will induce residual stresses in the tubes which can be seen when viewed under polarized light. Examination of the tubes employed in the highest power tests showed only slight traces of residual stresses. Thus, it is believed that the surface temperature of the fused silica tube did not exceed 1800 F even during the highest power tests. It was further assumed that the effective length for conduction heat flow was 3.0 in. (The discharge length is 2.0 in., but convective heating of the fused silica wall will likely occur over a slightly longer length.) Based on these assumptions, Q_C was calculated to be equal to 9.0 kw. This value for Q_C was used for the data shown in Fig. 2 where Q_T is ≥ 100 kw.

H-910093-44

For those tests in which $Q_T \leq 100$ kw, Q_C was assumed to be negligible. The maximum value of radiant flux achieved to date was 36.7 kw/in.^2 which corresponds to an equivalent black-body radiating temperature of 10,200 R.

The variation of power density with total discharge power is presented in Fig. 3. The maximum power density achieved was 322 kw/in.^3 (a 36 percent increase over that previously obtained) at a discharge pressure of 10 atm and a total discharge power of 177 kw.

The effect of discharge pressure on the fraction of the total energy transferred through the peripheral wall is shown in Fig. 4. The maximum discharge pressure reached was 16 atm in a test with a total discharge power of 113 kw.

Spectral emission measurements for several test conditions were completed to obtain an estimate of the temperature distribution in the plasma. The optical system and spectrometer employed are described in Ref. 2. However, for the current measurement the 100μ slit located between the plasma and monochromator entrance slit was replaced with a 27.5 in. focal length lens. Wavelength scans were made at $1000\text{\AA}/\text{min}$. The photomultiplier output was processed and recorded on a Model 1108 visicorder. The wavelength scans covered the 3800\AA to 8500\AA range. Figure 5 shows the radial variation of temperature for two test conditions. These temperatures were determined from the observed chordal variation in intensity of the Argon 4158.59\AA spectral line. The dashed line in Fig. 5 corresponds to a relatively low-power, low-pressure test condition, while the solid line corresponds to a test condition at increased power and pressure. As expected, the peak temperature occurs away from the discharge centerline. The small difference in temperature associated with both cases may be due to the compensating effects of simultaneous increase in power and pressure.

A chemical analysis and measurements of the optical transmissivity properties of the nigrosine dye were completed. Samples taken before, during, and after exposure to the intense radiation and r-f field indicated no change in the absorptivity properties of the nigrosine. (i.e., no decomposition or bleaching of the dye occurred.) In addition, separate tests were conducted to ascertain the effect of the r-f field on possible dye heating due to r-f coupling. These tests proved negative. Separate tests were also completed on the water used in the closed-loop cooling systems to verify minimum sodium content. Separate calibration tests were also completed to verify that no coating of dye occurred on the fused silica tubes due to decomposition of the dye or electrophoretic effects.

200- and 500-Atm Test Facility

The overall design and major component layout assembly of the 200-atm closed-loop r-f plasma test facility has been completed. This includes: an overall layout of the entire system including the master control console, an assembly drawing of the glass filament-wound test chamber, and an assembly

H-910093-44

drawing of the submersible pump and motor within their pressure vessel. Based on specification information and a detailed assembly drawing forwarded to the United Technology Corporation (Division of UAC) filament-wound motor case division, a positive concurrence was received as to the feasibility and practicability of fabricating a glass filament-wound high-pressure test chamber on a stainless steel mandrel as called out by our specifications. The system and test chamber were designed to be compatible with the existing end walls and the advanced transparent-wall models. A complete sizing of all major components together with the available source for possible procurement has also been finalized. Also included is a stress and factor-of-safety analysis of all the high-pressure system components.

The overall layout of a similar system capable of steady-state operation up to and including 500 atm has also been completed.

Transparent-Wall Model Research
(P. G. Vogt)

Transparent-Wall Model Tests in 1.2-Megw R-F Heater

During the report period, tests using a 0.010-in.-wall-thickness axial-coolant-tube model were conducted in the 1.2-megw r-f induction heater. The model consisted of 39 - 0.060-in.-OD x 0.040-in.-ID fused silica coolant tubes and 3 - 0.1875-in.-OD x 0.1275-in.-ID copper injector tubes located around a 1.2-in. diameter. The coolant tubes were potted into aluminum manifolds using silicone rubber. The injector tubes passed through these manifolds, and each has 14 - 0.020-in.-dia holes at an 11-deg injection angle for vortex injection.

The model is shown in Fig. 6a installed in the 1.2-megw r-f heater test section. A photograph of the plasma discharge during a typical test condition is shown in Fig. 6b. The power deposited in the discharge during these tests was approximately 20 kw. A summary of flow conditions and heat balance data is presented in Table II. Of the 20 kw approximately 24 percent was deposited in the annular coolant flow; approximately 35 percent was deposited in the water coolant for the 0.060-in.-OD model tubes, and approximately 28 percent was radiated out of the test chamber. The remainder was deposited in the end-wall and thru-flow coolant fluids. The amount of power indicated in the annular cooling passage, Q_w , is inaccurate due to the small (less than 3-deg) rise in coolant temperature which occurred during this test. The test series was terminated after approximately 1 hr of continuous running when a teflon injector outlet line blew off of one injector tube. A polyethylene sleeve on the connecting fitting softened and the teflon line blew out of the end-wall flange. The transparent-wall model was not severely damaged during the shutdown and will be used for further tests.

H-910093-44

In preparation for the next test series, a filter has been installed in the coolant water system to provide clean water (dirt particles which could lead to a plugged tube and cause burnout were noted in the coolant tubes following the test). If bypass argon flow is found desirable in the next test series, a measured amount of flow will be removed through ports drilled into the end wall flanges. Also, the flow of coolant in the annular passage will be reduced to allow a greater temperature rise to provide increased accuracy for calorimetric measurements.

Transparent-Wall Model Development

A 0.005-in.-wall-thickness axial coolant tube model is currently being readied for testing. In addition, models are being fabricated for testing with the propellant heater in the 1.2-megw r-f heater during the next report period.

Components for a 0.020-in.-wall-thickness circumferential model have been received and the first internally-cooled circumferential coolant tube model is being assembled.

Simulated Propellant Heating (J. F. Klein)

Fabrication of the propellant heating duct configuration and end walls for the 1.2-megw r-f induction heater was completed during this report period (see Fig. 10 of Quarterly Progress Report No. 22). This configuration now is being prepared for installation in the 1.2 megw r-f heater.

A propellant heating duct for use with the d-c arc was also fabricated during this report period. A sketch of this configuration is shown in Fig. 7. The arc is contained within a water-cooled quartz tube. The propellant heating duct is formed by two concentric fused silica tubes surrounding the water cooling passage for the arc. Results of initial tests to determine the radiation characteristics of the d-c source for propellant heating tests are presented in Fig. 8. The power radiated from the test section was measured directly, while the arc power within the test section was determined by assuming uniform arc power per unit length. The total arc power was approximately 3.8 times that within the test section.

The major objective in the tests to be conducted in both the d-c and 1.2 megw facility is to measure the temperature rise in the propellant stream. Secondary objectives are to measure the attenuation of arc radiation, to measure the various gas flow rates, and to observe the condition of the transparent walls before, during, and after the introduction of the carbon seeds. Tests conducted in the d-c arc facility at low power have indicated a moderate temperature rise in the propellant stream, and a corresponding attenuation of the radiation transmitted

H-910093-44

through the test section. Some coating of the quartz walls was also observed. A sketch of the time history of the propellant exhaust temperature and the transmitted radiation for a typical low-power test is shown in Fig. 9. Tests at higher radiation fluxes using the 1.2-megw r-f heater will be initiated soon. Inspection of the fused silica tubes employed in the d-c propellant heating tests showed that the aluminum coating, which is located on the inside of the fused silica tube separating the water cooling and propellant passages, blistered and peeled off over approximately 60 percent of the surface. It is not clear at this time if this is due to inadequate cooling or to poor coating quality.

Supporting Investigations of Vortex Fluid Mechanics
(A. E. Mensing, J. F. Jaminet and J. F. Klein)

R-F Heated Gas Vortex Tests

During this report period, the primary emphasis of gas tests in the 80-kw r-f induction heater has been two-component heated gas tests. In these tests, argon is employed as the simulated buffer gas and xenon as the simulated fuel. Most of the tests conducted in this quarter have been with the end-wall-driven vortex tube (see Figs. 13 and 14 of Quarterly Progress Report No. 22). This configuration consists of a 1.25-in.-ID fused silica tube as the peripheral wall of the vortex. The end walls are spaced 2.9 in. apart, and each end wall has four 0.044-in.-ID argon injector tubes located at a radius of 0.50 in. The flow conditions listed in Table III of Quarterly Progress Report No. 22 resulted in a plasma, ellipsoidal in shape, having a maximum diameter of 0.80 in. midway between the end walls and tapering to a minimum diameter of 0.3 in. next to each end wall.

It was noted in the previous progress report that, when xenon was injected into the argon plasma, pulsations of the plasma occurred whenever the xenon flow rates exceeded certain values. These pulsations have been eliminated by detuning the r-f coupling network to reduce the reflected impedance of the plasma. This decreased the efficiency (defined as r-f power divided by d-c plate power) from 70 percent to approximately 50 percent and, of course, required greater d-c plate power to maintain a given power to the plasma. However, xenon flow rates up to 5 percent of the argon flow rate have been obtained with no pulsation or unsteadiness of the plasma occurring.

Gas discharge tests using tungsten particle seeds were conducted in both the 80-kw and 1.2-megw r-f induction heaters. Vortex configurations having end-wall seed injection ports were used in both test series. While some visible and spectral evidence of the presence of tungsten in the discharge was obtained, only a slight increase in discharge radiation was measured. Based on these tests it was concluded that the seed material injected from the end wall was not entering the discharge. No further tests with particle seeds are planned until the results of tests using gaseous seeds to find the best place for seed injection are completed.

Tests were conducted in which xenon was injected into the argon plasma through each of four different locations. The presence of xenon was determined both by a change in the r-f resonator voltage and by the strength of the $\text{XeI}4671$ spectral line. The four xenon injection methods were: (1) premixed with the argon prior to injection into the vortex, (2) through a port in one end wall, normal to the end wall, and at a radius of 0.38 in., (3) through a port normal to the peripheral wall, midway between the end walls, and protruding approximately 1/8 in. through the wall, and (4) through a water-cooled probe, 0.18-in.-OD, located on the vortex centerline and protruding into the plasma.

Premixing xenon with argon prior to injection into the vortex was used as a reference since it is assumed that the xenon and argon are completely mixed within the plasma. To detect the xenon emission lines, (primarily the $\text{XeI}4671$ and $\text{XeII}4844$) the xenon partial pressure within the plasma must be greater than approximately 0.005 atm. For conditions of these experiments this means the xenon mass flow rate must be at least 2 percent of the argon mass flow rate. For a standard condition, a xenon mass flow rate of approximately 4 percent of the argon was chosen. The addition of xenon at this rate results in a resonator voltage decrease of approximately 25 percent and a corresponding decrease in power to the plasma. The intensity of the $\text{XeI}4671$ line is then approximately the same as the $\text{ArI}4300$ line.

When xenon was injected through a port in one end wall, port diameters of 0.040 and 0.020 in. were used and the xenon injection velocities were varied from 20 to 400 ft/sec. (It was necessary to add some argon to the xenon to obtain the increased velocities.) Using this method, xenon was not detected either optically (i.e., by emission) or electrically (i.e., by change in resonator voltage) until the injection velocity was great enough to severely alter the plasma shape. Even under these conditions the amount of xenon that appeared within the plasma was much less than for the premixed case, thus suggesting time constant ratios much less than 1.0. Thus, this method of injecting a heavy gas appears very undesirable.

A 0.040-in.-ID fused silica tube, located normal to the peripheral wall, was also used to inject xenon. Some argon was mixed with the xenon to increase the velocity out the tube. With this configuration and with a xenon flow rate approximately the same as for the premixed case, xenon was detected in the plasma both electrically and by line emission. In fact, the xenon line strength was two to three times stronger than the premixed case, and the resonator voltage was 5 to 10 percent lower than the premixed case. Power to the plasma also appeared to decrease. Increasing the xenon injection velocity to greater than about 100 ft/sec tended to cut the plasma into two distinct halves with a dark region at the plane of injection. Thus, providing the injection velocity is not too great, this method of injection appears quite promising and is to be investigated further.

A water-cooled probe is constructed that was inserted in one thru-flow port into the plasma. Xenon was injected up the center of this probe. The probe was small enough so that it did not appreciably restrict the exhausting flow, nor did it have any effect on the plasma coupling. Initially, with the probe tip flush with the end wall, the injected xenon appeared to make a 180-degree turn and would not enter the plasma core. The probe was pushed in until the tip was about $5/8$ in. from the end wall. With the probe in this position, xenon was detected optically in the plasma. However, there was virtually no change in resonator voltage nor in power to the plasma. Since the plasma power and, hence, temperature remained high, it is difficult at this stage to relate xenon line strength to xenon concentration. Several chordal scans of the $\text{XeI}4671$ line at different axial locations showed the xenon was present throughout the plasma. Even $1/8$ -in. downstream of the tip, the xenon extended radially to about 80 percent of the plasma edge, 20 times larger than the xenon injection port diameter. Thus, the jet appears to expand very rapidly. Chordal scans further downstream of the probe tip showed the xenon emission increased from the tip to a point approximately midway between the tip and the far end wall, then decreased as the end wall was approached. This latter effect could be caused by a temperature decrease in the argon plasma as the end wall is approached. This method of injecting into a plasma is also to be investigated further. It is important to note that this method had a negligible effect on the r-f coupling. This phenomenon coupled with the observations of decreased coupling in both the premixed case and the peripheral-wall case suggests that, in the latter cases, some of the xenon is ionizing outside the plasma, but is at too low a temperature to be detected optically.

Tests are presently being conducted in which quantitative data relative to the spatial distribution of the xenon density within the plasma are being determined. These tests will include only three of the four aforementioned injection methods. Xenon injection through a port in the end wall is not promising enough to warrant further investigation at the present time.

Additional tests were conducted with the peripheral-wall simulated buffer injection configuration discussed in Quarterly Progress Report No. 22 and shown in Fig. 12 of that report. This method of attaching copper injectors to a fused silica tube was somewhat more successful than the original method discussed in Quarterly Progress Report Nos. 21 and 22. However, the close proximity of the injector to the r-f work coil led to severe arcing and eventual failure of the fused silica tube. A new tube has been fabricated and will be tested with a larger diameter r-f work coil. Tests with this configuration and with xenon as the simulated fuel are to be conducted in the near future.

An investigation was begun during this report period to determine if radioactive techniques could be used in measuring the density of a simulated fuel. The study showed that the use of a radioactive "tag" gas (such as $\text{XeI}33$) was

prohibitively expensive, but that Compton scattering of gamma rays from a 1 Mev source may be a useful technique. A small experiment has been set up using the corporate-owned 0.662 Mev Cs137 source and scintillation counter. Several predetermined mixtures of xenon and argon have been made up and tests are presently in progress to determine if the scattering technique will have either the sensitivity or resolution necessary for two-component heated gas vortex tests.

Two-Component Isothermal Gas Vortex Tests

During this report period, additional improvements in the high Reynolds number test facility have been accomplished. (This facility is described in Appendix IV of Ref. 2.) A modification was made which allows a maximum of 55 percent of the inlet flow to be bypassed through the vortex tube. The axial light absorption system scanner was relocated in a plane normal to the axis of the vortex tube, eliminating the need for one set of mirrors, thus reducing alignment difficulties. Finally, the data recording system has been completely calibrated and quantitative data are now being obtained. Although the latest data are not available for this report, some qualitative observations can be mentioned.

Two buffer gas injection configurations were qualitatively investigated: (1) peripheral-wall injection from 56 injection ports, arranged in 2 rows 180 deg apart, and (2) end-wall tangential injection from 4 ports at each end wall, located at $r/r_0 = 0.8$. The total buffer gas injection areas for both configurations were approximately equal. The injection areas and locations were determined from the areas employed in the 80-kw facility through use of the parameters $\frac{2r_{01}}{A_j}$ and r/r_0 . Values of the parameters were approximately equal for both the 80-kw and high Reynolds number configurations. Although the simulated fuel injection ports also were located by this method, the area of the fuel injection ports was sized to provide reasonable fuel injection velocities and fuel-to-buffer-gas weight flow ratios.

Results of tests with peripheral-wall injection were similar to those reported previously. The radial location of the stagnation streamline decreased with increasing tangential injection Reynolds number and increased with axial bypass. With a sufficiently high percentage of bypass flow, an annular ring containing simulated fuel was formed.

With end-wall vortex injection, a very unsatisfactory vortex was formed. Simulated fuel was concentrated along the axis of the vortex tube and virtually nonexistent everywhere else. Axial bypass increased the core volume of simulated fuel somewhat, but no well-defined stagnation streamline or annular ring was generated. In contrast, this configuration resulted in a stable plasma in the r-f heated gas vortex tests described in preceding subsections. Reasons for the apparent differences in results obtained from heated and unheated tests are currently being investigated.

COAXIAL-FLOW TESTS
(B. V. Johnson)

During this report period, the studies were directed toward determining the effect of inlet configuration on the apparent inner-jet gas containment volume. Tests with the foam inlets and $r_I = 3.0$ and 3.5 in. indicated the inner-jet gas was diluted or contracted upstream of the inlet plane for high weight-flow-rate ratios. The apparent containment was approximately the same as obtained and reported previously for the foam inlet with $r_I = 2.5$ in. However, a modification of the inlet to prevent dilution or contraction of the inner-jet gas upstream of the inlet plane resulted in an increase of the apparent inner gas containment volume by more than a factor of two compared to previous results.

Sketches of the inlet configurations employed in the previous and the present coaxial-flow tests are shown in Fig. 10. The screen inlet, Fig. 10a, was that described in Ref. 3. The velocity profiles measured $\frac{1}{2}$ in. downstream from the inlet plane had "step" changes in the indicated velocity profile between the inner-jet and buffer-stream regions and between the buffer-stream and outer-stream regions. Flow visualization studies employing this inlet indicated that large eddies were formed downstream of the inlet plane causing large-scale mixing (Ref. 3). The foam inlet (Fig. 10b) was used to smooth the velocity discontinuity at the inlet by allowing the flow from the inlet manifolds to flow through a porous media ($\frac{1}{2}$ -in.-thick foam) before entering the chamber at the inlet plane. Results from flow visualization tests and velocity profile measurements, reported in Quarterly Progress Reports Nos. 21 and 22, indicate that smooth inlet velocity profiles were obtained and elimination of the large-scale mixing of the inner-jet gas was accomplished with the foam inlet. However, the apparent containment of inner-jet gas in the chamber was not appreciably changed (Quarterly Progress Report No. 22). In order to improve the containment characteristics, the foam inlet was modified to prevent radial flow of the outer-stream gas toward the center in the foam at radii less than r_I . The inner-jet inlet duct was extended to the inlet plane and was covered with a perforated plate to prevent counter-flow at the inlet plane (Fig. 10c). Results from flow visualization tests with the foam and perforated plate inlet for $r_I = 3.0$ in. indicated that improvement in the apparent containment was obtained. However, the high-speed motion pictures indicated that small-scale eddies formed at the edge of the inner-jet gas regions. A comparison of the apparent containment for tests with Freon-11 as the inner-jet gas and these three inlet configurations is shown in Fig. 11. The results for the screen inlet and foam inlet with $r_I = 2.5$ in. are those reported in Quarterly Progress Report No. 22. The apparent containment was obtained from the axial variation of the outermost radius of the high concentration inner-jet gas (colored with iodine vapor). For the foam inlet with $r_I = 3.0$ in., the apparent containment was approximately the

H-910093-44

same as for the foam inlet with $r_I = 2.5$ in. and the screen inlet with $r_I = 2.5$ in. For the foam and perforated plate inlet and $r_I = 3.0$ in., the apparent containment for $W_{BAO}/W_I > 20$ was approximately twice as much as obtained with the screen inlet or foam inlet. The flagged symbols for this case indicate that recirculation was beginning to occur near the nozzle. Based on previous studies (Ref. 3), the decrease in containment due to the observed recirculation is expected to be less than 20 percent of the indicated value.

RADIANT HEAT TRANSFER CALCULATIONS OF
SPECTRUM FROM FUEL
(N. L. Krascella)

Calculations were initiated to ascertain the spectral radiant flux emitted from the fuel region of a nuclear light bulb rocket engine. These calculations were based on an iterative procedure utilizing the UARL simplified grey-gas and spectral transport computer codes. The procedure is analogous to that used previously to determine radiative transfer in the propellant region of a gaseous nuclear rocket engine (Refs. 4 and 5).

Two cases were considered for the initial calculations. These cases differ in the ionization potentials assigned to the various nuclear fuel ionization species, as summarized in Table III. In both cases studied, the effective black-body radiating temperature was assumed to be approximately 15,000 R. The effective total radiative flux corresponding to this temperature is 24,300 Btu/ft²-sec. This total radiative flux was assumed constant in the fuel-containment region (see following paragraph). The iterative procedure was continued until the total flux, obtained by integrating the spectral flux from the spectral computer code, was equal to 24,300 Btu/ft²-sec, \pm 10 percent. In both cases the fuel partial pressure distribution illustrated in Fig. 12 was used. Similarly, an edge-of-fuel temperature of 12,650 R was assumed for both cases.

Nine iterations have been completed for both cases to date. Typical temperature distributions (calculated by means of the simplified grey-gas computer code) for both cases are shown in Fig. 13 for the 8th and 9th iterations as a function of distance from the edge of the fuel. These temperature distributions and the fuel partial pressure distribution of Fig. 12 were used in the spectral computer code to calculate spectral absorption coefficients, the spectral energy flux and, finally, the total energy flux.

Typical spectral absorption coefficient data for temperatures of 12,650, 14,650, and 19,650 R are shown in Fig. 14 as a function of wave number for both cases. The data at a temperature of 12,650 R represent the spectral absorption coefficient at the assumed edge-of-fuel temperature (12,650 R). (The edge-of-fuel temperature should theoretically be equal to $(2)^{-\frac{1}{4}}$ times the black-body radiating temperature if there is no return flux to the fuel.) The total flux obtained by integrating the spectral flux computed with the spectral computer code is shown in Fig. 15 as a function of distance from the edge of the fuel. Results are illustrated for the last two iterations (8th and 9th) for cases 1 and 2. The results show that convergence was effectively accomplished except for the last few points near the edge of the fuel. The iterative procedure will be continued until the end points converge.

The spectral flux calculated at the edge-of-fuel temperature (12,650 R) is shown in Fig. 16 for the last iteration (9th) for both cases as a function of wave number. The black-body spectral flux at a temperature of 15,000 R (approximately the effective radiating temperature) is also shown for comparison. It should be noted that the spectral flux at the edge-of-fuel temperature is slightly less than the black-body flux for cases 1 and 2 up to a wave number of approximately 30,000 cm^{-1} . At wave numbers greater than about 30,000 cm^{-1} the emitted spectral flux is greater than that of a black body at a temperature of 15,000 R. It should be noted, however, that the total flux for cases 1 and 2 in the 9th iteration and at the edge-of-fuel temperature are about 10 percent greater than that of a black body at the effective radiating temperature of 15,000 R (see Fig. 15).

The reason for specifying a constant total flux in Fig. 15 can now be understood by examining the results shown in Figs. 12, 13, 14 and 16. The spectral absorption coefficients are sufficiently high that the spectral flux is governed by the temperatures existing in approximately the outer 1-cm layer of fuel. The ratio of the fuel stored in this 1-cm layer to the total fuel stored is approximately 0.02. Since the neutron flux is approximately constant throughout the fuel region, the flux at $y = 1$ cm should be approximately 2 percent less than that at $y = 0$. However, even with 9 iterations (see Fig. 15), it has not been possible to specify a temperature distribution that will keep flux constant within 2 percent; therefore, specifying a constant flux in this region, rather than one which changes by 2 percent, is a permissible approximation.

The spectral energy flux calculations were made in the wave number range between 10^3 and 10^6 cm^{-1} . It is of interest to know the fractional distribution of energy between these wave number limits. The fractional distribution of energy between the lower wave number limit (10^3 cm^{-1}) and any wave number ω , as well as the fractional distribution between the upper wave number limit (10^6 cm^{-1}) and any wave number w , are shown in Fig. 17. Results are illustrated at the edge-of-fuel temperature of 12,650 R for cases 1 and 2. These results are for the last or 9th iteration. For comparison, similar results are illustrated for a black body at a temperature of 15,000 R. The results show that in both cases approximately 50 percent of the energy radiated is at wave numbers less than approximately 30,000 cm^{-1} . For a black body at the effective radiating temperature, 50 percent of the energy radiated is below a wave number of approximately 20,000 cm^{-1} .

Of particular interest is the energy radiated at a wave number greater than 60,000 cm^{-1} (wavelength less than 0.17 microns), where fused silica becomes highly opaque. According to Fig. 17, the energy above 60,000 cm^{-1} is between 18 and 26 percent of the total energy, whereas only 1.6 percent of the black-body spectrum is above this wave number. If this energy were absorbed, it would be a severe heat load on the transparent wall. However, as noted in preceding reports, it should be possible to seed the flow so as to increase the opacity at high wave numbers. For example, the addition of neon will effectively eliminate all radiant energy emitted

H-910093-44

above a wave number of $170,000 \text{ cm}^{-1}$ (the ionization potential of neon), and the addition of a relatively small amount of argon to the entire flow would effectively eliminate all radiant energy emitted above a wave number of $127,000 \text{ cm}^{-1}$ (the ionization potential of argon). Neither of these effects has been considered in the analysis discussed in this progress report.

During the next quarter, additional cases using the ionization potential data of case 2 (see Table III) will be considered in which walls of varying reflectivity will be incorporated in the calculational procedure.

MEASUREMENT OF OPTICAL TRANSMISSION DURING REACTOR IRRADIATION
(R. M. Gagosz and G. R. Palma)

Efforts during the current report period were concentrated in the following major areas:

- a) Electron irradiation experiments conducted at the NASA Space Radiation Effects Laboratory at Newport News, Virginia, from April 22 to May 2. The spectral transmission characteristics of Corning 7940 fused silica were measured during irradiation by 1.5 Mev electrons from a Dynamitron linear accelerator. Post irradiation spectral scans and optical bleaching experiments were also performed using these electron-irradiated specimens.
- b) Scheduling of the proposed steady-state neutron irradiation experiments. Preliminary discussions have been held with reactor personnel at the Nuclear Engineering Center of Wright Patterson AFB.

Electron Irradiation Experiments

Further electron irradiation experiments were performed at the Virginia Associated Research Center, Newport News, Virginia, during the current report period. The optical transmission of Corning Grade 7940 fused silica was measured during irradiation by 1.5 Mev electrons from a Dynamitron linear electron accelerator. The experimental arrangement was similar to that used in the previous electron irradiation experiments described in detail in the previous progress report. Several problems were encountered in the previous electron irradiation experiments that necessitated certain modifications to the electron accelerator and the specimen furnace. The previous experiments did not yield equilibrium data at the nominal ionizing flux of 150 microamps/cm² due to fluctuations in the output of the electron accelerator. In addition, the specimen furnace used in the previous experiments did not permit rapid temperature control over a sufficient range independent of the electron heating. These limitations resulted in nonequilibrium data at low flux and low temperature which was difficult to interpret and of limited use in the simulation of a nuclear light bulb rocket engine. Since the last test period, modifications have been made to the electron accelerator, consisting of a new power supply and redesigned output window, which resulted in steady-state electron beam outputs at current densities as high as 150 microamps/cm² for periods of time as long as 1000 sec. A new specimen furnace was designed which could be used to vary the specimen temperature during steady-state electron irradiation in order to obtain

information on the variation of induced absorption coefficient with specimen temperature at constant electron flu.. With these modifications it was possible to obtain measurements of the radiation-induced absorption coefficient at $\lambda = 2150\text{\AA}$ for a wide range of electron flux (20-150 microamps/cm²) and specimen temperatures (170-930 C).

A total of 16 electron accelerator runs were made during the period from April 22 to May 2, of which five were used for calibration purposes. A single optical transmission run was made at a wavelength of 4500\AA , an electron current density of 80 microamp/cm², and a specimen temperature of 560 C. No equilibrium absorption was observed at this wavelength. The 10 remaining optical transmission runs were made at $\lambda = 2150\text{\AA}$, the center of the largest radiation-induced absorption band observed in preceding tests.

Plots of the induced absorption coefficient, Dynamitron electron current density, furnace power and specimen temperature as functions of elapsed time have been made for all of the runs, and the plots for runs 10, 14, and 15 are included as Figs. 18, 19, and 20, respectively. The Dynamitron electron current density is controlled manually by the Dynamitron operator. The turn-on time of the electron beam is usually about 1 to 10 sec as shown in Fig. 20 although in run 14 (Fig. 19) there was a period of about 100 sec during which a small current of 1 to 5 microamps was present after which the electron beam was turned on full in a period of 10 sec. Difficulties in maintaining steady high current densities were sometimes encountered by the Dynamitron operator. After a certain period of steady-state operation, the electron beam current would decrease; this behavior was only encountered in one of the optical transmission runs, (run 14), and is illustrated in Fig. 20. The furnace power was changed by the UARL operator in a time of approximately 5 sec. The Dynamitron current directly heats the specimen, resulting in a change of specimen temperature governed by a time constant of from 50 to 150 sec, depending on the magnitude of the electron current density, while changing the furnace power resulted in a change in specimen temperature governed by a time constant of approximately 200 sec.

It can be seen from Figs. 18 through 20 that an increase in absorption coefficient during irradiation generally results from either an increase in Dynamitron current or a decrease in specimen temperature. However, in several of the runs, the absorption coefficient was found to increase after the Dynamitron current was turned off, as shown in Figs. 19 and 20. This behavior had been observed in previous Dynamitron experiments and represents an anomaly in the data at present. Figures 18 and 20 exhibit an overshoot phenomena in that the induced absorption coefficient reaches a maximum value before returning to a lower equilibrium value. This is due to the fact that the turn-on of the Dynamitron current occurs rapidly, while the rise in sample temperature occurs more slowly.

The equilibrium values of induced absorption coefficient obtained during all runs are plotted against specimen temperature for different values of electron current density in Fig. 21. The measured equilibrium induced absorption coefficient varies from near zero at 20 microamps/cm² and 450 C to 12.1 cm⁻¹ at 100 microamps/cm² and 600 C. Of particular interest is the measured induced absorption coefficient of 12.0 cm⁻¹ at an electron current density of 150 microamps/cm² (which simulates the rocket engine ionizing flux) and a specimen temperature of 930 C. As can be seen from Fig. 21, there was insufficient control of specimen temperature to obtain data at a fixed temperature for a wide range of electron currents. However, a preliminary indication of the effect of changes in electron current at a given temperature can be obtained by extrapolating each of the data curves in Fig. 21 to a specimen temperature of 500 C. If this is done, an unexpected indication is obtained that the induced absorption coefficient varies approximately as the cube of the electron current density. However, the data are certainly not yet sufficiently complete to draw conclusions from such extrapolations.

Post-irradiation spectral scans were made on all of the previously irradiated specimens over a range of wavelengths from 2150Å to 3000Å. All of the spectral scans indicated a pronounced absorption band at $\lambda = 2150\text{\AA}$ with some specimens showing a smaller band in the range 2500Å - 2700Å. These bands overlap in general so that it is difficult to determine the width of the individual absorption bands accurately in each case. However, in those cases where only the single band at $\lambda = 2150\text{\AA}$ was present, the measured half-width of the band was approximately 300Å.

The time for the induced absorption coefficient to decay to 1/e of its original value as a result of optical bleaching was determined in a post-irradiation experiment with specimen number 4 using a hydrogen lamp as a light source and found to be 4800 sec. Since the photon flux in this experiment was approximately 10^{-7} of that expected in a full-scale nuclear rocket engine, the expected optical bleaching time constant in the full-scale nuclear rocket engine is approximately 0.48×10^{-3} sec. In order for optical bleaching to be effective, the time constant for creation of coloration must be longer than 0.48×10^{-3} sec. No measurements of this time constant for creation of coloration have yet been made. The most reliable way to determine the effects of optical bleaching would be to conduct an irradiation experiment that included a high-intensity light source so that measurements of induced absorption coefficient could be made as a function of light intensity as well as radiation flux and specimen temperature.

Steady-State Neutron Irradiation Experiments

Progress on scheduling the proposed steady-state neutron irradiation experiments was delayed when the Union Carbide Safety Committee failed to approve the proposed experiments in their present form. The Committee was concerned about the possibility of a water leak; Union Carbide is unwilling to shut down the reactor in the

H-910093-44

event of such a leak because of the effect on other experiments. The reactor supervisor estimates that it would take about 5 months to make the necessary modifications to guarantee approval by the Safety Committee. In view of the difficulties encountered in attempting to schedule the experiments at Union Carbide, a search for an alternate reactor facility was conducted. The most likely candidate for the proposed neutron irradiation experiments is presently the Nuclear Engineering Center at Wright-Patterson Air Force Base, Dayton, Ohio. Discussions with reactor personnel indicate that this facility can supply neutron and gamma dose rates at least as high as those expected from the Union Carbide facility, and that no serious problems of safety or compatibility exist, since they are willing to shut down the reactor in the unlikely event of a water leak. A tentative schedule, subject to final approval by the Nuclear Engineering Center's Safety Committee, has been devised which calls for three weeks of experiments beginning July 28.

ENGINE DESIGN

(T. S. Latham, H. E. Bauer and R. J. Rodgers)

Engine Dynamics

The calculation procedure for use in analyzing the dynamic response of the NLB engine is being developed by combining the systems of equations which describe the behavior of the three coolant circuits in the engine with the neutron kinetics equations. The cavity coolant circuit, the secondary hydrogen coolant circuit, and the hydrogen propellant circuit are being analyzed, programmed and checked separately and will be combined for the study of overall engine transients. Investigations of the secondary hydrogen coolant circuit have been completed and sample results are discussed below. The hydrogen propellant circuit equations have been programmed and are presently being checked. The cavity coolant circuit is being analyzed in a simplified form pending further specific design work on such components as fuel and fission product separators. The neutron kinetics equations shown in Fig. 11 of Ref. 8 have been expanded to include reactivity feedbacks due to changes in moderator temperature, propellant and coolant density, and average fuel residence time. The expanded neutron kinetics equations have been programmed and checked out in preparation for inclusion in an entire engine simulation program.

The interfaces between the three coolant circuits are the heat exchangers and the turbopumps. The programs for the separate circuits are designed to permit feedback through those components for each time step. The anticipated procedure is to calculate the coolant temperature levels throughout the engine for each time step, apply these temperatures to the calculation of pressure losses, bulk moderator temperatures and turbopump characteristics so that reactivity coefficients, flow variations and changes in physical properties may be calculated.

A schematic diagram of the secondary hydrogen coolant circuit used in the transient analysis is shown in Fig. 22. This simplified circuit differs from the circuit shown in Quarterly Progress Report No. 21 in that the pressure vessel and the upper and lower end walls have been combined as a single heat source. Also, the tie rods and flow divider have been combined with the liner tubes as a single heat source, and the cavity coolant circuit heat exchanger has been removed from the secondary coolant circuit and included in the hydrogen propellant circuit. The combination of the components mentioned above does not change the transient response of the secondary coolant circuit to any great degree since the heat deposition in the end walls, tie rods and flow divider is approximately 10 percent of the total secondary coolant circuit heat deposition and these components are combined with major components which have similar time response characteristics and similar coolant residence times.

In order to isolate the secondary coolant circuit from the remainder of the engine, it was necessary to assume that all of the heat deposited in the secondary coolant would be rejected in the primary-to-secondary circuit heat exchanger (component 204, Fig. 22) so that the temperature at the heat exchanger outlet (location 2045, Fig. 22) is essentially constant. It was also assumed that there was no appreciable change in the secondary circuit pressure loss or in the secondary pump speed so that the flow rate in the secondary circuit was constant. The equations used to describe the heat exchanger and pump characteristics have provisions for varying these values when the appropriate inputs are available from the equations describing the remaining coolant circuits.

The response of local temperature levels in the secondary coolant circuit to a 10 percent step increase in power level is shown in Fig. 23. The response to a 10 percent step decrease in power level is shown in Fig. 24. The effect of the coolant residence time in each component may be seen from the slope of the outlet temperature variation. The additional time lag which may be noted in the heat exchanger inlet temperature (location 2040, Fig. 22) is due to the time required for the coolant to travel from the transparent wall outlet, which is located at the upper end of the unit cavities, to the heat exchanger which is in the upper end of the pressure vessel.

The percentage change in the temperature rise in each component is equal to the percentage change in power level with the exception of the transparent wall during a positive power excursion. This difference is a result of a nonlinear variation in the radiant heat absorption rate in the transparent walls, which is a function of the fuel radiating temperature and the absorption coefficient of the transparent wall. An equation for the variation of the radiation heat load in the transparent walls as a function of fuel radiating temperature was developed from data given in Ref. 9. The data indicated that the radiation heat load was proportional to the fourth power of the fuel radiating temperature if the fuel radiating temperature is below 15,000 R. If the fuel radiating temperature is above 15,000 R, the change in the absorption coefficient causes the radiation heat load to increase more rapidly with temperature, becoming approximately proportional to the ninth power of the fuel radiating temperature. Since the fuel radiating temperature is proportional to the fourth root of the engine power level, a combination of the equations for radiating temperature and radiation heat load indicates that the radiation heat load to the transparent walls is directly proportional to the power variation for radiating temperatures less than 15,000 R and proportional to the $9/4$ power of the power variation for radiating temperatures in excess of 15,000 R.

Since the radiation heat load is on the order of one half of the total heat deposited in the transparent walls, the overall effect of a positive 10 percent step change in power level is approximately a 15 percent increase in the temperature rise in the transparent wall.

Engine Start-Up

Studies of engine start-up concepts were initiated. Three forms of fuel are under consideration: particles, UF_6 , and molten uranium. UF_6 and particles show merit as start-up fuels, while either particles or liquid uranium appear suitable for full-power operation.

The start-up steps are as follows: (1) close nozzle (it was shown in Ref. 10 that a variable-throat-area nozzle would be necessary to limit the flow rate of propellant during start-up); (2) fill both the hydrogen ducts and the neon system from storage until its neon density is equal to the neon injection density at nominal full power operation (0.926 lb/ft^3 , or a pressure of 17.7 atm at room temperature); (3) turn-on neon recirculation pump, (4) inject fuel particles or UF_6 until critical mass is reached; (5) increase power level and adjust flow rates and pressures to maintain criticality and pressure balance throughout the system and to limit component temperatures to desirable levels; (6) inject propellant seeds at about 10 percent of full power (this occurs at an equivalent black-body radiating temperature of 8500 R, at which point the exhaust nozzle is nearly in the full-open position); and (7) raise power to desired level.

Thus far, work has been concentrated on step (5). To make the studies tractable, it has been assumed that start-up can be controlled such that power will increase on a linear ramp from 0 power to 10 percent of full power (460 megw). Two start-up rates are under consideration: a linear power ramp rising to 460 megw in 1 min, and a linear power ramp rising to 460 megw in 10 min. It has also been assumed that the fission energy is deposited uniformly in the fuel cloud. Equations have been derived which describe the energy balance in a unit cell during the start-up process. At low powers, the loss rate of energy from the fuel region is governed by conduction and convection, with convection being the principal energy loss mechanism, while at high powers, radiation becomes the dominant energy loss mechanism.

Data have been obtained describing the physical properties and compositions of fuels, buffer gas, and propellant over the range of temperatures and pressures of interest. The energy balance equations will be programmed shortly to obtain the required temperature, pressure, and flow rate time histories during the start-up power ramps. Criticality calculations for several points during the start-up power ramp will also be made to determine the fuel injection rates required during the start-up process.

Design of Pewee In-Reactor Test

Results of studies directed toward determining the feasibility of testing a nuclear light bulb model employing a fissioning gas in a Pewee type test reactor were presented to Los Alamos staff members. The results presented included drawings

of a reference design flux trap, drawings and lists of alterations to the basic Pewee reactor design required to insert a flux trap, and data describing the level of performance and types of demonstration tests which could be performed. Briefly, the results indicated that nuclear light bulb demonstration tests could be performed in a Pewee type reactor with a central flux trap in which the surface radiating temperature might reach 14,600 R at vortex region pressures of 500 atm. The dimensions of the test region would be approximately 3 in. in diameter and 15 in. long.

Several suggestions were made by Los Alamos staff members. The principal item of concern was that the effluent from the vortex test region had to be piped through the center of the exhaust nozzle into a region where the piping would be exposed to the high heat loads in the exhaust plume. To avoid this, it was suggested that the possibility of placing the NLB test vortex in the Pewee reflector be investigated. Preliminary investigations of thermal neutron flux levels indicate that performance levels in the reflector region would be essentially the same as in a central flux trap. Examination of the assembly drawings also indicates that a demonstration test could be placed in the reflector with the effluent from the test piped out through the pressure vessel near the nozzle throat such that exposure to the exhaust plume could be avoided. Insertion of an NLB demonstration test in the Pewee reflector will be included as one of the test options in the interim summary report.

Another suggestion was made to explore the possibility of constructing a small test reactor with a flux trap made of zirconium hydride which might require far fewer Pewee fuel elements. It was found from exploratory one-dimensional calculations that a small configuration could be designed which would go critical with approximately 126 Pewee fuel elements. However, the peak thermal neutron fluxes achievable would restrict performance levels of a test to surface radiating temperatures less than 10,000 R. Because of the reduced performance, it has been decided to drop the possibility of a small configuration as an NLB demonstration test reactor option.

MISCELLANEOUS

The following visited the Research Laboratories during the reporting period to discuss one or more phases of gaseous nuclear rocket technology:

April 28, 1969 - Captain C. E. Franklin of the Space Nuclear Propulsion Office

June 10, 1969 - Mr. F. C. Schwenk and Captain C. E. Franklin from the Space Nuclear Propulsion Office

In addition, one or more phases of gaseous nuclear rocket technology were discussed during the following trips:

April 1, 1969 - Los Alamos Scientific Laboratory (Messrs. W. Martin, K. Boyer, H. Knight, V. Zeigler, F. Durham, J. Farr, J. Weinbrecht, K. Cooper, C. Bankston, D. Blevins, J. Cully, H. Newman, W. Kirk, J. Orndoff, D. Hanson, J. Rowley, J. Sapir, R. Schreiber, G. Jarvis, and C. Landahl from LASL and Captain C. E. Franklin from the Space Nuclear Propulsion Office)

April 15, 1969 - University of Illinois, Urbana, Illinois; seminar entitled "Research on the Nuclear Light Bulb Gaseous-Core Reactor."

May 1, 1969 - Space Nuclear Propulsion Office (Mr. F. C. Schwenk and Captain C. E. Franklin)

REFERENCES

1. Mensing, A. E. and L. R. Boedeker: Theoretical Investigations of R-F Induction Heated Plasmas. United Aircraft Research Laboratories Report G-910091-18, prepared under Contract NASw-847, September 1968. Also issued as NASA CR-1312.
2. Kendall, J. S., W. C. Roman and P. G. Vogt: Initial Radio-Frequency Gas Heating Experiments to Simulate the Thermal Environment in a Nuclear Light Bulb Reactor. United Aircraft Research Laboratories Report G-910091-17, prepared under Contract NASw-847, September 1968. Also issued as NASA CR-1311.
3. Johnson, B. V.: Experimental Study of Multi-Component Coaxial-Flow Jets in Short Chambers. United Aircraft Research Laboratories Report G-910091-16, prepared under Contract NASw-847, April 1968. Also issued as NASA CR-1190.
4. McLafferty, G. H. and W. G. Burwell: Theoretical Investigation of the Temperature Distribution in the Propellant Region of a Vortex-Stabilized Gaseous Nuclear Rocket. United Aircraft Research Laboratories Report C-910093-10, prepared under Contract NASw-847, September 1964. Also issued as NASA CR-279.
5. Kesten, A. S. and R. B. Kinney: Theoretical Effect of Changes in Constituent Opacities on Radiant Heat Transfer in a Vortex-Stabilized Gaseous Nuclear Rocket. United Aircraft Research Laboratories Report D-910092-5, prepared under Contract NASw-847, September 1965.
6. Williamson, H. A., H. H. Michels and S. B. Schneiderman: Theoretical Investigation of the Lowest Five Ionization Potentials of Uranium. United Aircraft Research Laboratories Report D-910099-2, prepared under Contract NASw-847, September 1965.
7. Waber, J. T., D. Liberman and D. T. Cromer: Unpublished Theoretical Ionization Potentials for Uranium. Los Alamos Scientific Laboratory, received June 1966.
8. Latham, T. S.: Nuclear Studies of the Nuclear Light Bulb Rocket Engine. United Aircraft Research Laboratories Report G-910375-3, prepared under Contract NASw-847, September 1968. Also issued as NASA CR-1315.
9. McLafferty, G. H.: Absorption of Thermal Radiation in the Transparent Wall of a Nuclear Light Bulb Rocket Engine. Journal of Spacecraft and Rockets, Vol. 4, No. 6, June 1967, pp. 758-761.
10. McLafferty, G. H. and H. E. Bauer: Studies of Specific Nuclear Light Bulb and Open-Cycle Gaseous Nuclear Rocket Engines. United Aircraft Research Laboratories Report F-910375-2, prepared under Contract NASw-847, September 1967. Also issued as NASA CR-1030.

LIST OF SYMBOLS

a_{ω}	Spectral absorption coefficient, cm^{-1}
A_j	Vortex tube injection area, sq in.
A_S	Discharge surface area, sq in.
d	Discharge diameter, in.
f	Frequency, MHz
l	Vortex tube length, in.
P	Reactor power, megw
P_D	Discharge pressure, atm
P_F	Partial pressure of nuclear fuel, atm
P_I	Total d-c input power to r-f heater, kw
Q^*	Effective black-body radiative flux, $\text{Btu/ft}^2\text{-sec}$
Q_C	Power conducted through peripheral wall, kw
Q_E	Power deposited in end-wall cooling water, kw
Q_R	Power measured by radiometer (see text), kw
$Q_{R,3}$	Power radiated through test section of d-c propellant heater duct
Q_T	Total discharge power, $(Q_R + Q_W + Q_E)$, kw or Total radiative flux = $Q_{\omega}d_{\omega}$, $\text{erg/cm}^2\text{-sec}$
$Q_{T,3}$	Fraction of total arc power in d-c test section
Q_{TF}	Power convected out of test chamber in thru-flow exhaust duct, kw
Q_W	Power deposited in peripheral wall coolant, kw
Q_{ω}	Spectral radiative flux, erg/cm-sec
r	Local radius from center of chamber, in. or ft

H-910093-44

LIST OF SYMBOLS
(cont'd)

r_B	Buffer-stream radius at inlet, in. or ft
r_I	Inner-jet radius at inlet, in. or ft
r_O	Peripheral-wall radius, in. or ft
T	Temperature, deg K or R
T_{AV}	Average temperature in plasma determined from measurements of radiated power, deg R
T_{BB}	Equivalent black-body radiating temperature, deg R
V	Discharge volume, in. ³ or local velocity, ft/sec
W_A	Argon weight flow, lb/sec
W_{BAO}	Weight flow rate of combined outer and buffer streams, lb/sec
W_I	Weight flow rate of inner jet, lb/sec
x	Distance from center of fuel containment region, cm
y	Distance from edge of fuel containment region, cm
η	R-F system coupling efficiency, Q_T/P_I , dimensionless
λ	Wavelength, micron
ϕ_R	Radiant energy flux $(Q_W + Q_R - Q_C)/A_S$, kw/sq in.
ω	Spectral wave number, cm ⁻¹

Subscript

0	Initial or reference condition
---	--------------------------------

TABLE I

CHARACTERISTICS OF HIGH POWER R-F LIGHT SOURCE

Discharge Geometry

Diameter, d	0.82 in.
Length, l	2.00 in.
Surface Area*, A_S	4.28 sq in.
Volume*, V	0.71 in. ³

Flow Conditions

Discharge Gas	Argon
Injection Flow Rate, W_A	0.03 lb/sec
Discharge Pressure, P_D	8.5 atm
Average Temperature, T_{Av}	20,500 R (see text)

R-F Parameters

Frequency, f	5.51 MHz
Total Input Power, P_I	600 kw
Total Discharge Power, Q_T	215 kw
Efficiency, η	35.8 percent

Power Dissipation

Power dissipated in peripheral-wall coolant, Q_W	147 kw
Power conducted through peripheral wall, Q_C	9.0 kw (see text)
Power deposited in end-wall cooling water, Q_E	47 kw

H-910093-44

TABLE I
(cont'd)

Power convected out of test chamber in thru-flow exhaust duct, Q_{TF}	3.0 kw
Power measured by radiometer, Q_R	18 kw
Power radiated through peripheral wall, $(Q_W + Q_R - Q_C)$	156 kw
Radiating flux based on discharge surface area, $\phi_R = (Q_W + Q_R - Q_C)/A_S$	36.7 kw/sq in.
Equivalent black-body radiating temperature, T_{BB}	10,200 R
Power density, Q_T/V	307 kw/in. ³

TABLE II

SUMMARY OF RESULTS FOR GAS DISCHARGE TEST
EMPLOYING TRANSPARENT-WALL MODEL

Test Conducted in 1.2-megw R-F Induction Heater
Photograph of Model Shown in Fig. 6

Flow Conditions

Discharge gas	Argon
Injection flow rate, W_A	0.012 lb/sec
Discharge pressure, P_D	4.6 atm
Discharge length, l	2.0 in.
Diameter of model	1.25 in.

Power Dissipation

	<u>Absolute Power, kw</u>	<u>Fraction of Total Power</u>
Total discharge power, Q_T	20.5	1.0
Power deposited in end wall cooling water, Q_E	2.6	0.13
Power deposited in water coolant in 0.060-OD fused silica tubes, Q_M	7.1	0.35
Power measured by radiometer, Q_R	5.8	0.28
Power deposited in annular cooling water, Q_W	5.0	0.24

H-910093-44

TABLE III

DATA USED IN CALCULATING SPECTRUM RADIATED FROM FUEL
(see Figs. 12 to 17)

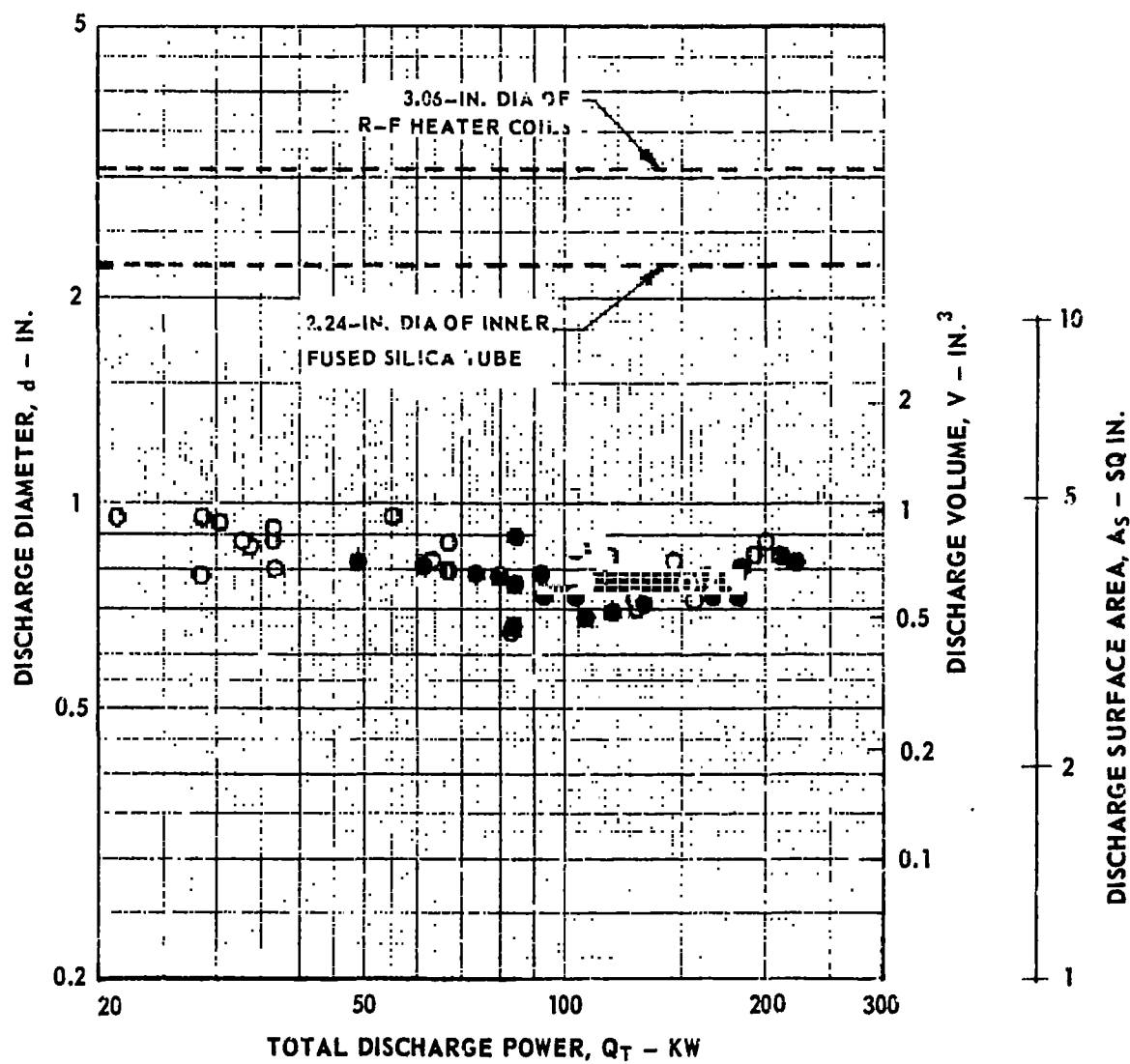
Case	Ionization Potentials, I.P. (ev)					Effective Black-Body Radiating Temperature, T_{BB} (deg R)	Total Flux at T_{BB} Btu/ft ² -sec
	UI	UII	UIII	UIV	Ref.		
1	6.1	17.1	38.8	65.6	6	15,000	24,300
2	6.11	11.46	17.94	31.14	7	15,000	24,300

GEOMETRIC CHARACTERISTICS OF DISCHARGES OBTAINED IN TESTS

RANGE OF DISCHARGE PRESSURE, $P_D = 2$ TO 16 ATM

RANGE OF ARGON WEIGHT FLOW, $W_A = 0.010$ TO 0.041 LB/SEC

SOLID SYMBOLS DENOTE SWIRL INJECTORS ON BOTH END WALLS

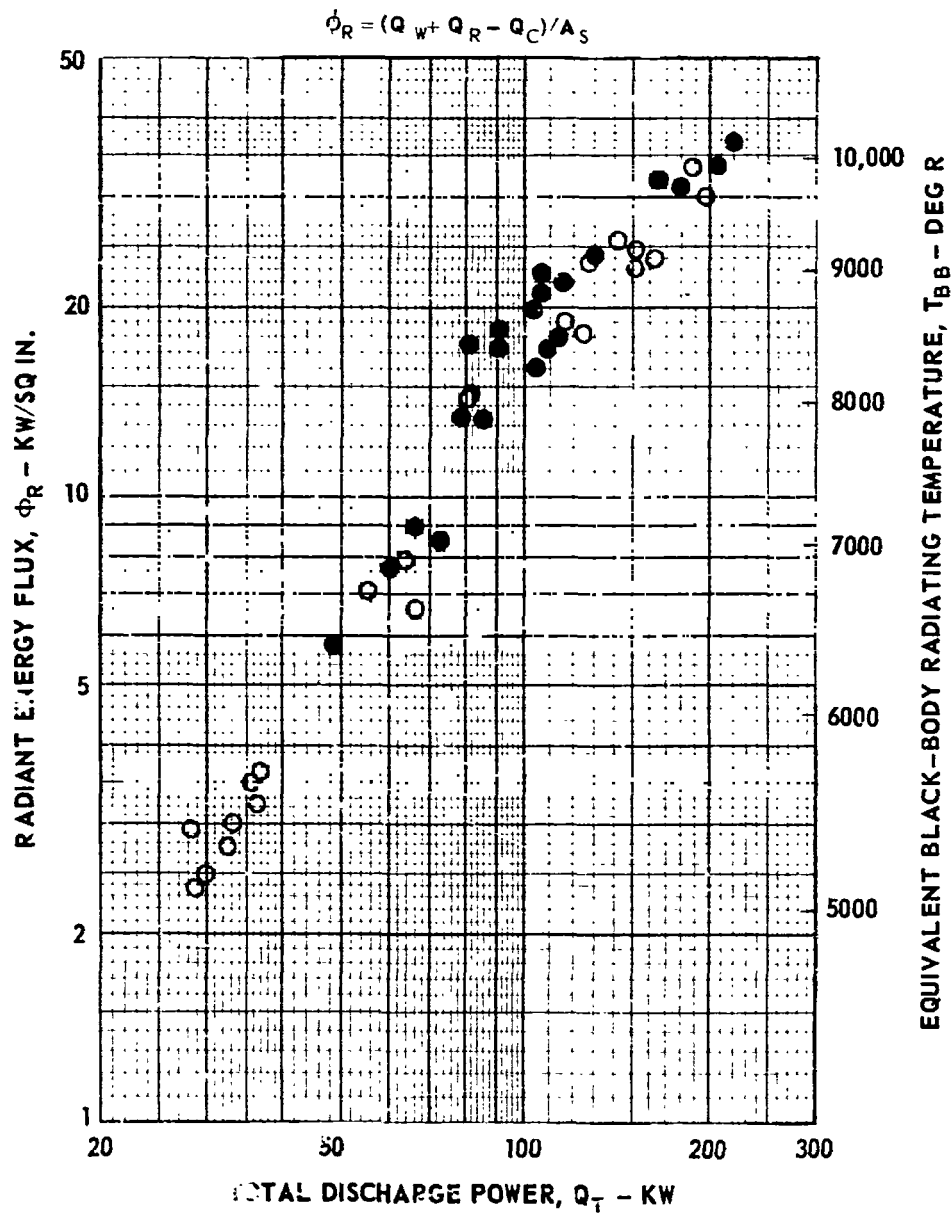


VARIATION OF RADIANT ENERGY FLUX WITH TOTAL DISCHARGE POWER

RANGE OF DISCHARGE PRESSURE, $P_D = 2$ TO 16 ATM

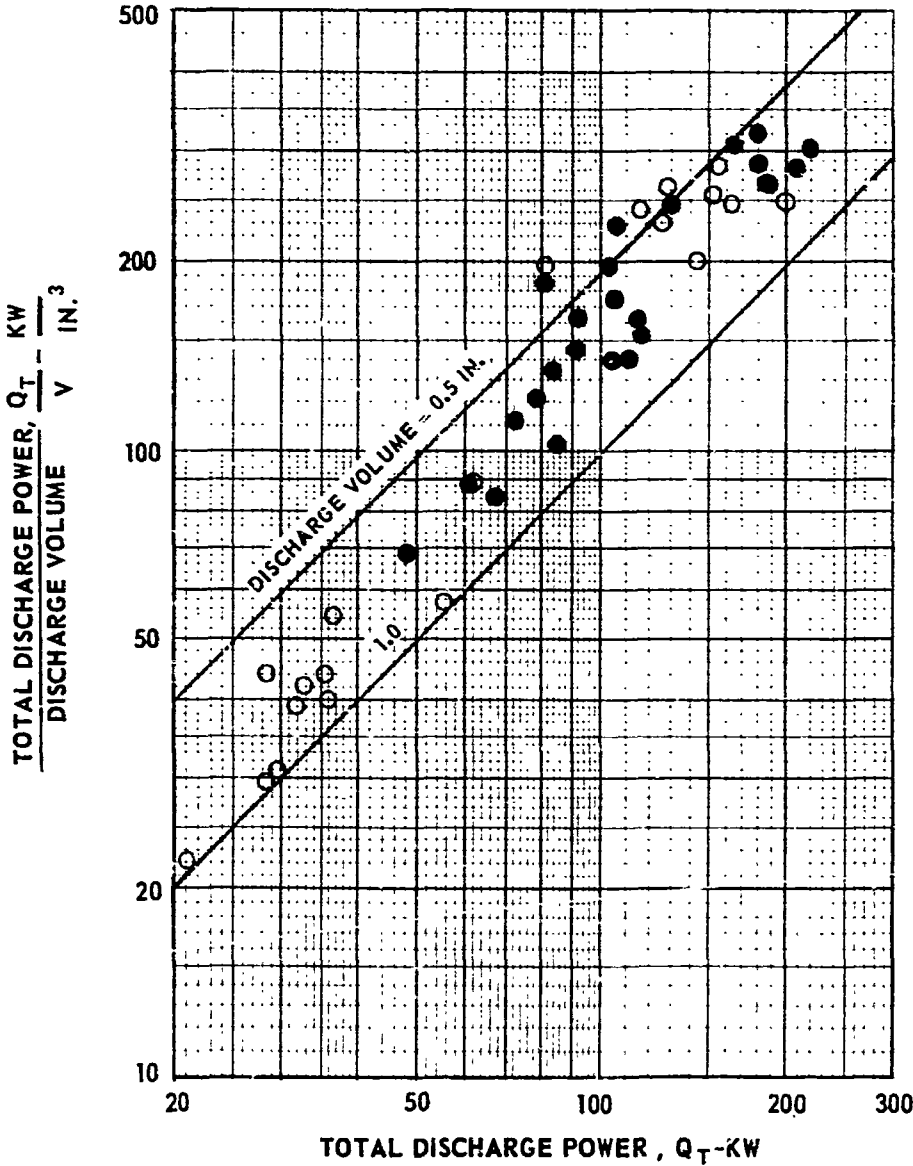
RANGE OF ARGON WEIGHT FLOW, $W_A = 0.010$ TO 0.041 LB/SEC

SOLID SYMBOLS DENOTE SWIRL INJECTORS ON BOTH END WALLS



VARIATION OF DISCHARGE POWER PER UNIT VOLUME WITH TOTAL DISCHARGE POWER

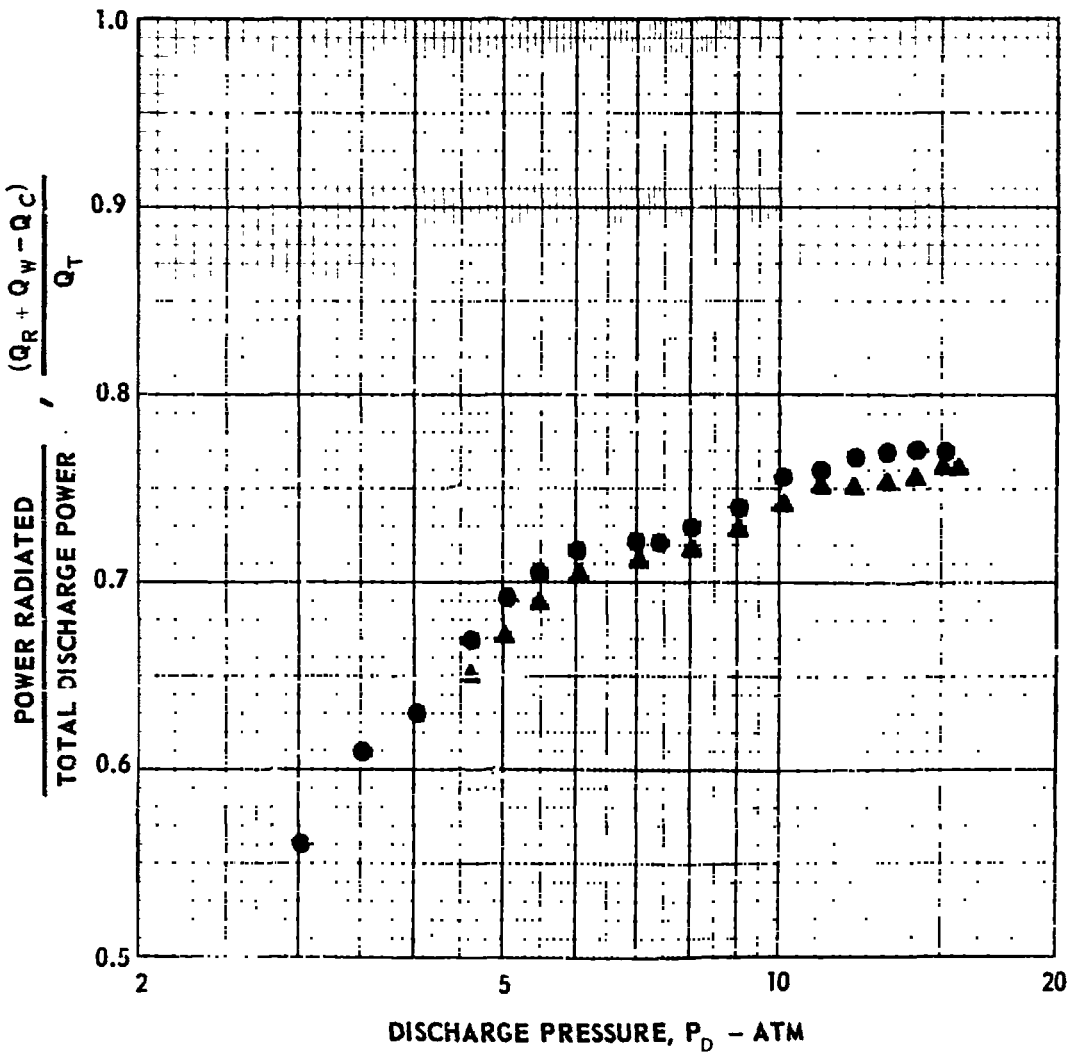
RANGE OF DISCHARGE PRESSURE, $P_D = 2$ TO 16 ATM
RANGE OF ARGON WEIGHT FLOW, $W_A = 0.010$ TO 0.041 LB/SEC
SOLID SYMBOLS DENOTE SWIRL INJECTORS ON BOTH END WALLS



EFFECT OF DISCHARGE PRESSURE ON FRACTION OF POWER RADIATED

RANGE OF TOTAL DISCHARGE POWER, $Q_T = 50$ TO 116 KW

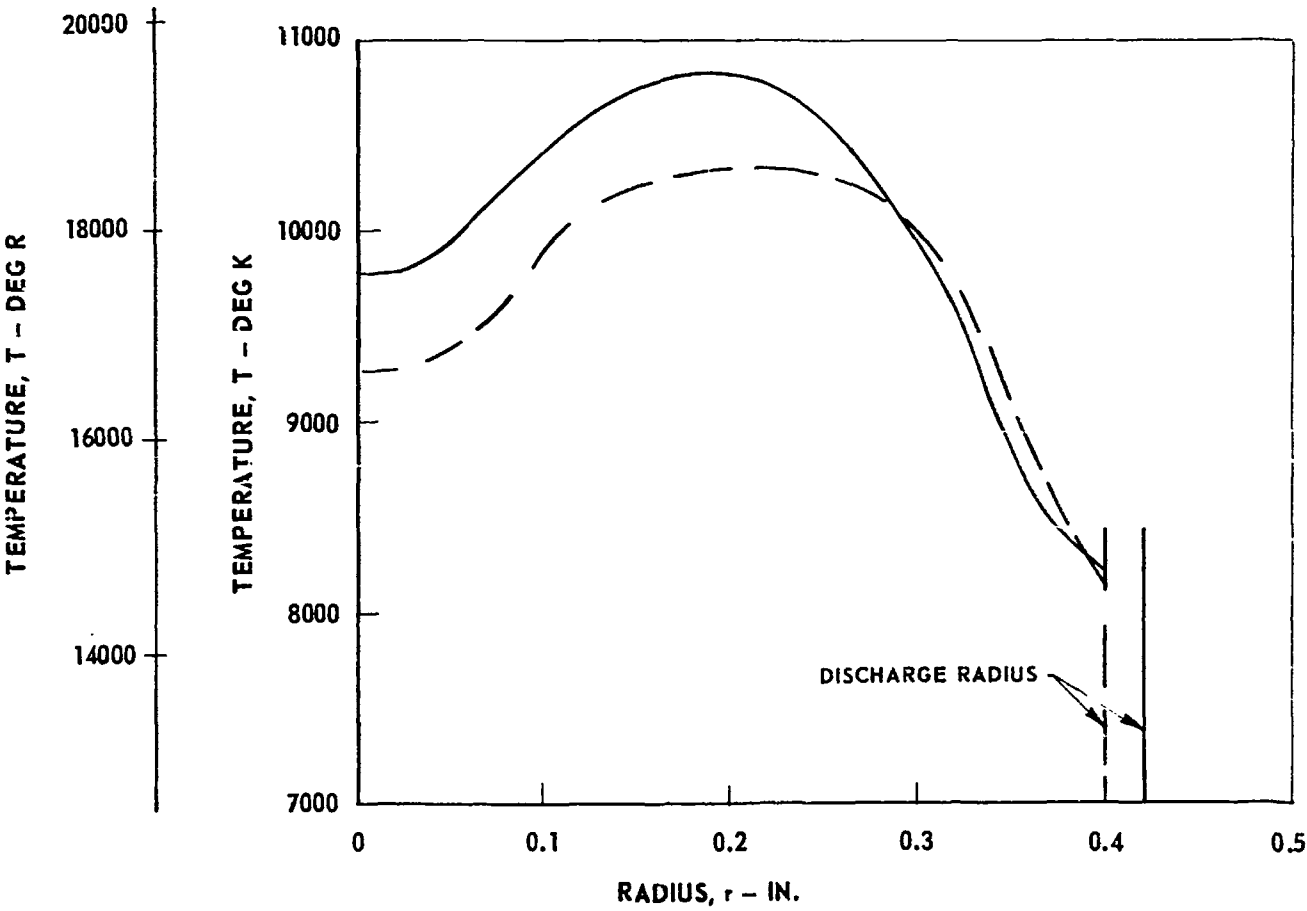
SYMBOL	ARGON WEIGHT FLOW, W_A — LB/SEC
▲	0.012
●	0.015



TYPICAL RADIAL DISTRIBUTIONS OF TEMPERATURE
OBTAINED IN GAS DISCHARGE TESTS

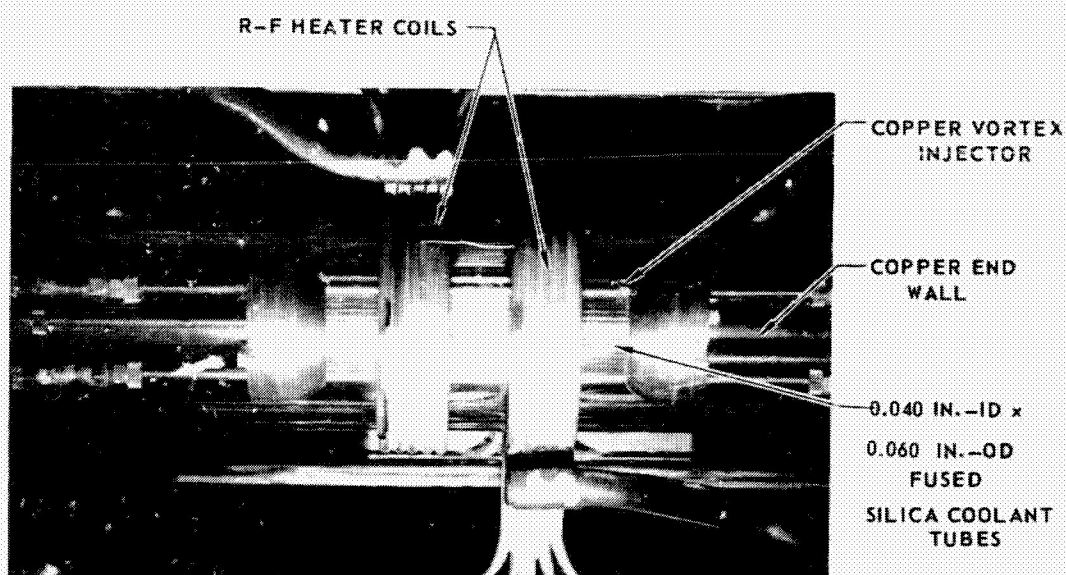
ARGON DISCHARGE
TEMPERATURE DETERMINED FROM INTENSITY OF ARGON 4158.59 Å LINE

— $P_D = 7 \text{ ATM}, Q_T = 120 \text{ KW}$
- - - $P_D = 4 \text{ ATM}, Q_T = 60 \text{ KW}$

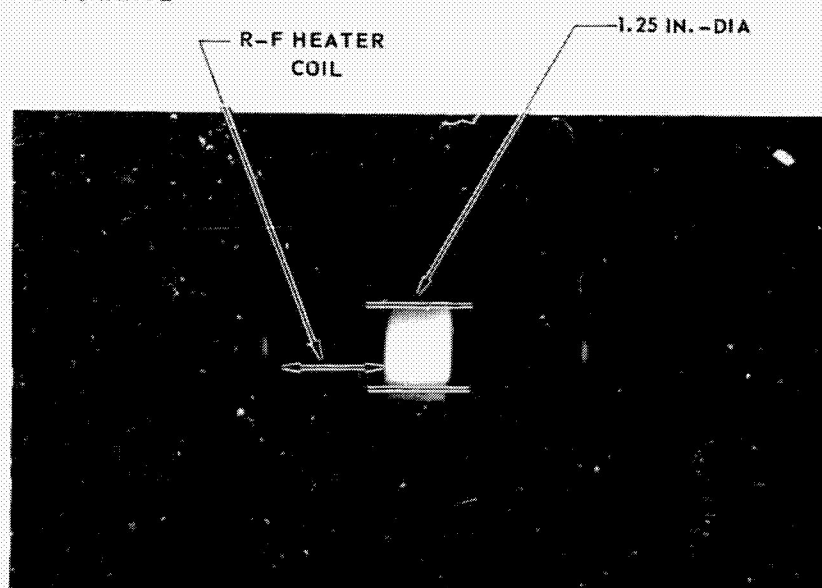


GEOMETRY OF TRANSPARENT-WALL MODEL EMPLOYED IN GAS DISCHARGE TESTS
SEE TABLE II FOR SUMMARY OF TEST RESULTS

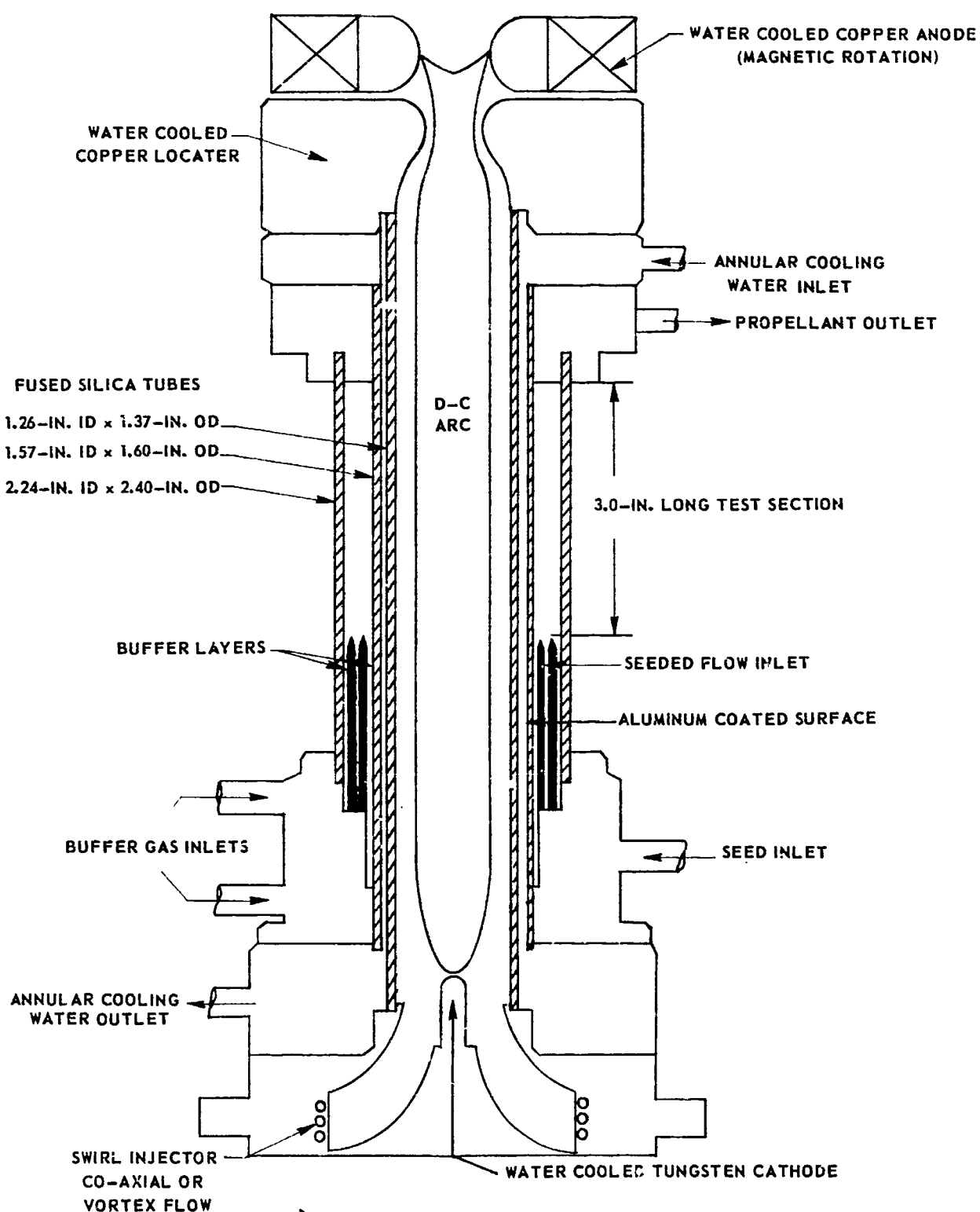
a) PHOTOGRAPH OF MODEL IN 1.2 MEGW R-F HEATER



b) PHOTOGRAPH OF DISCHARGE

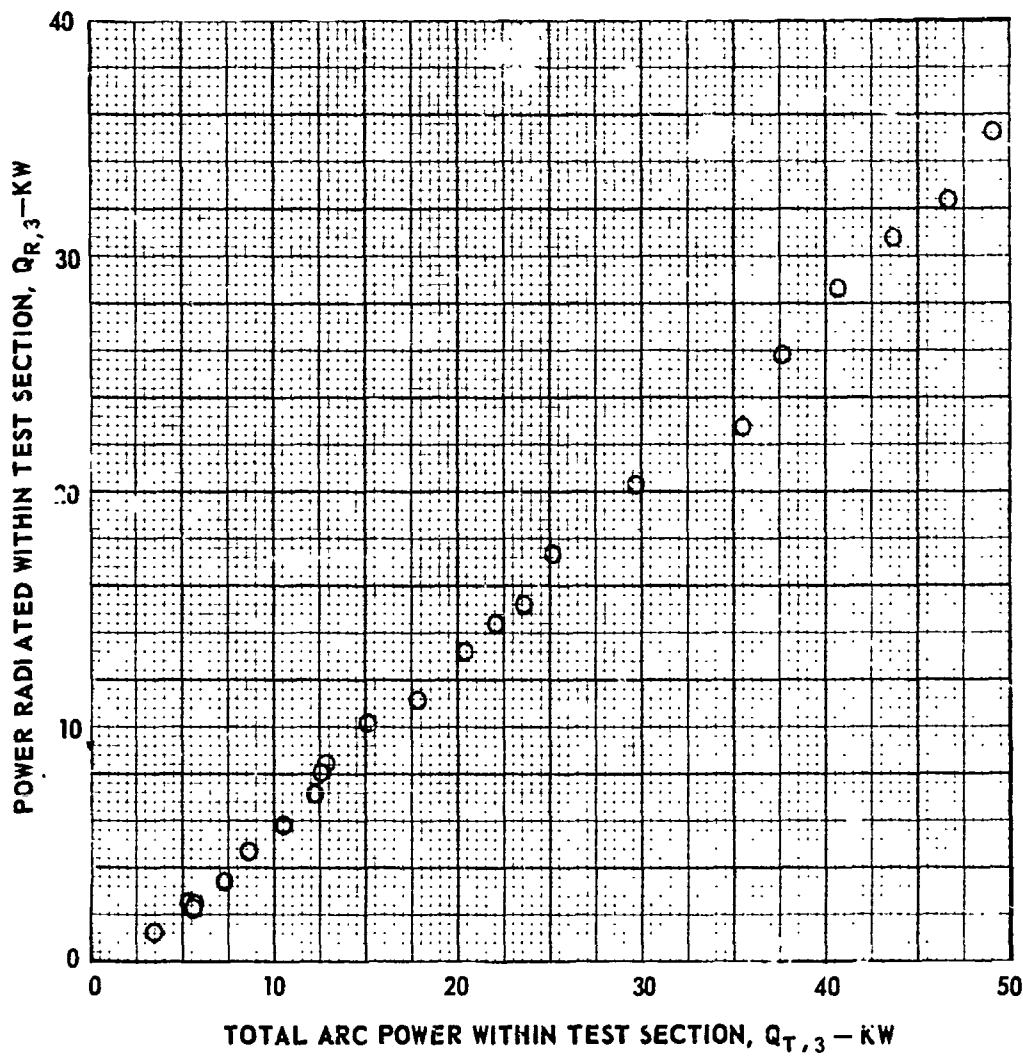


SKETCH OF PROPELLANT HEATING DUCT CONFIGURATION FOR TESTS USING D-C ARC SOURCE



CHARACTERISTICS OF D-C ARC SOURCE USED
IN SIMULATED PROPELLANT HEATING TESTS

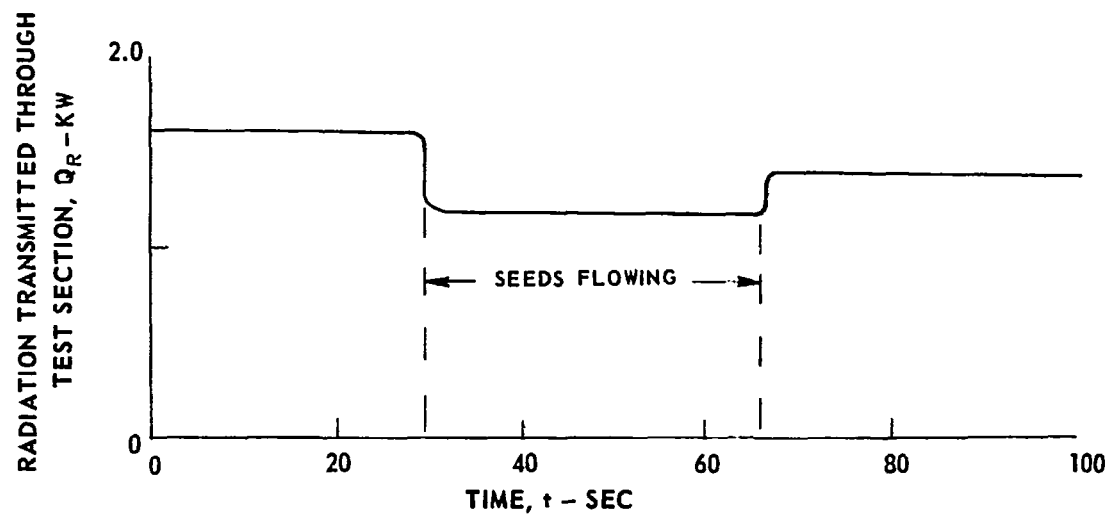
SEE FIG. 7 FOR TEST SECTION DETAILS



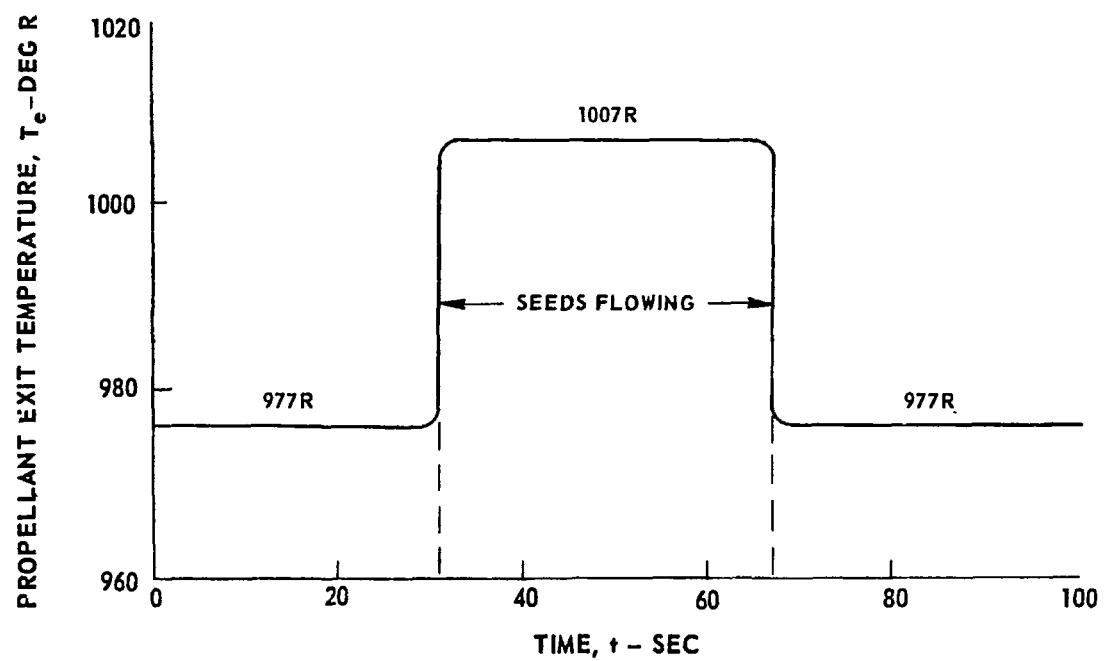
RESULTS OF INITIAL PROPELLANT HEATING TESTS USING D-C ARC SOURCE

DETAILS OF CONFIGURATION GIVEN IN FIG. 7

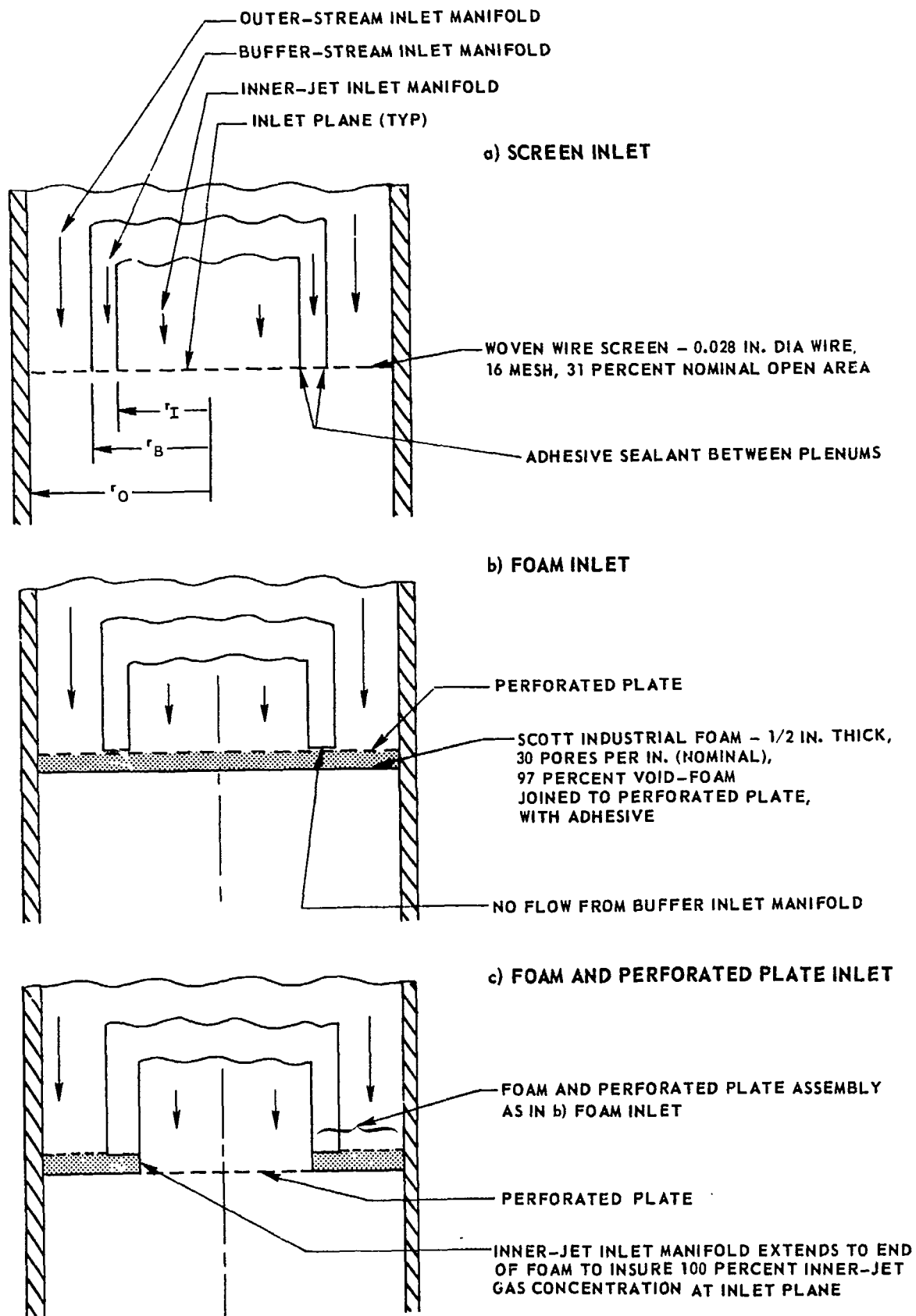
a) TRANSMITTED RADIATION



b) SIMULATED PROPELLANT EXIT TEMPERATURE



SKETCHES OF INLET CONFIGURATIONS EMPLOYED IN COAXIAL-FLOW TESTS


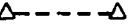
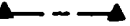



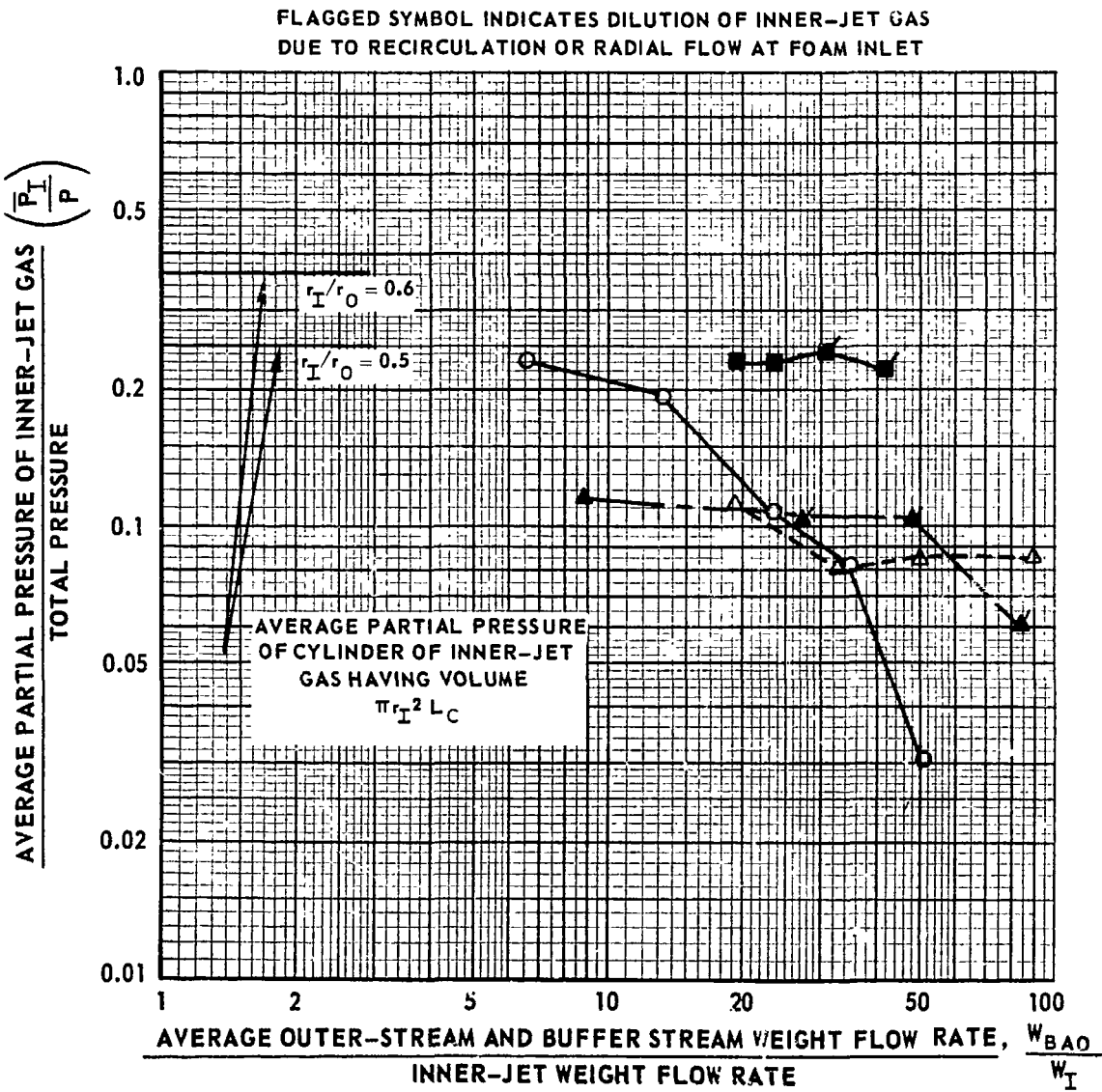
COMPARISON OF APPARENT COAXIAL-FLOW CONTAINMENT FOR SEVERAL INLET CONFIGURATIONS

FIG. 11

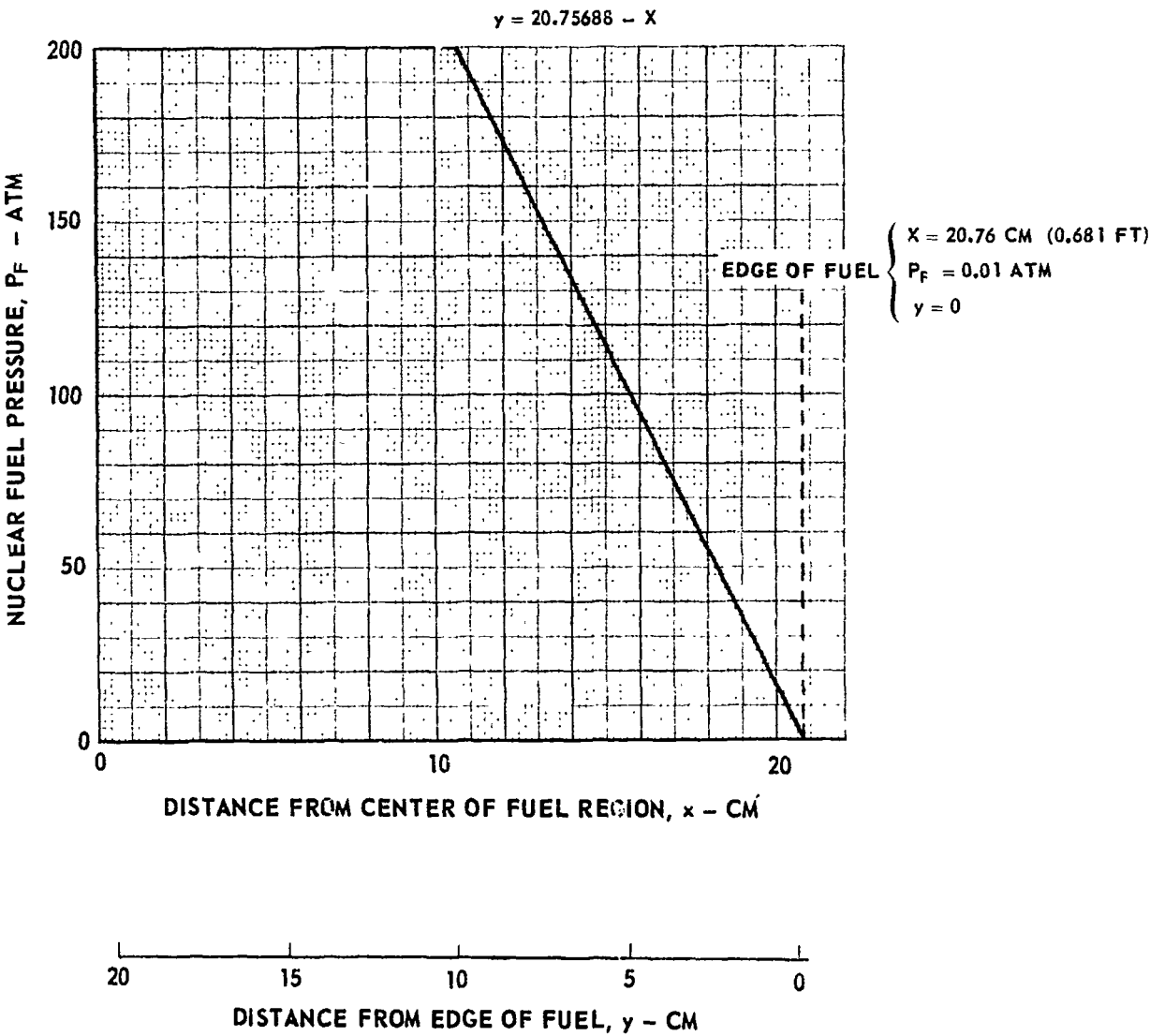
BUFFER AND OUTER GAS - AIR
INNER-JET GAS-FREON-11

$\rho_{BAO}/\rho_I \approx 4.7$

SYMBOL	INLET CONFIGURATION	r_I IN.	r_B , IN.	DATA OBTAINED
	a) SCREEN	2.50	3.25	REF. 3
	b) FOAM	2.50	3.25	PHOTOGRAPHS
	b)FOAM	3.00	3.63	PHOTOGRAPHS
	c) FOAM AND PERFORATED PLATE	3.00	3.63	PHOTOGRAPHS

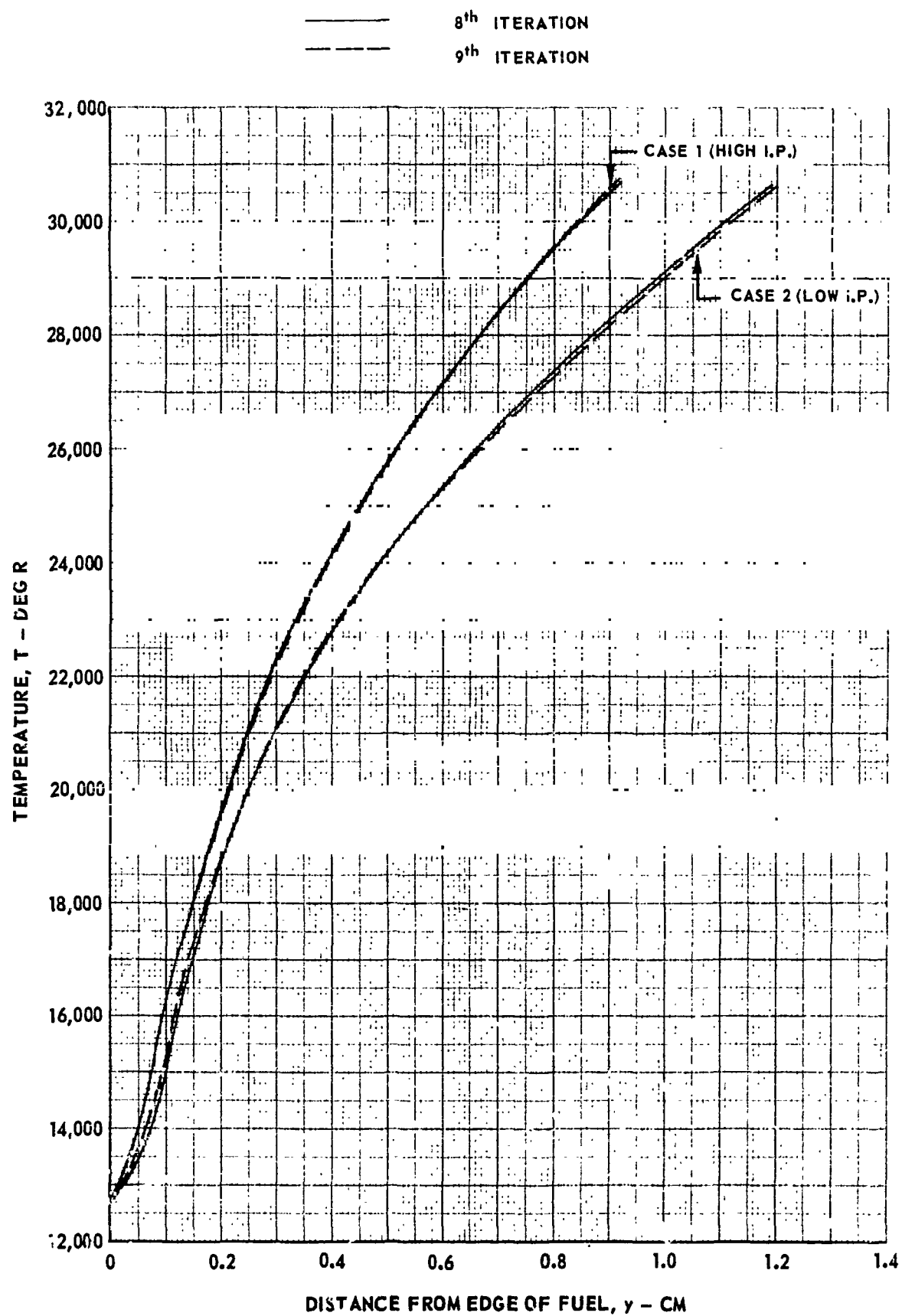


PARTIAL PRESSURE DISTRIBUTION IN FUEL REGION

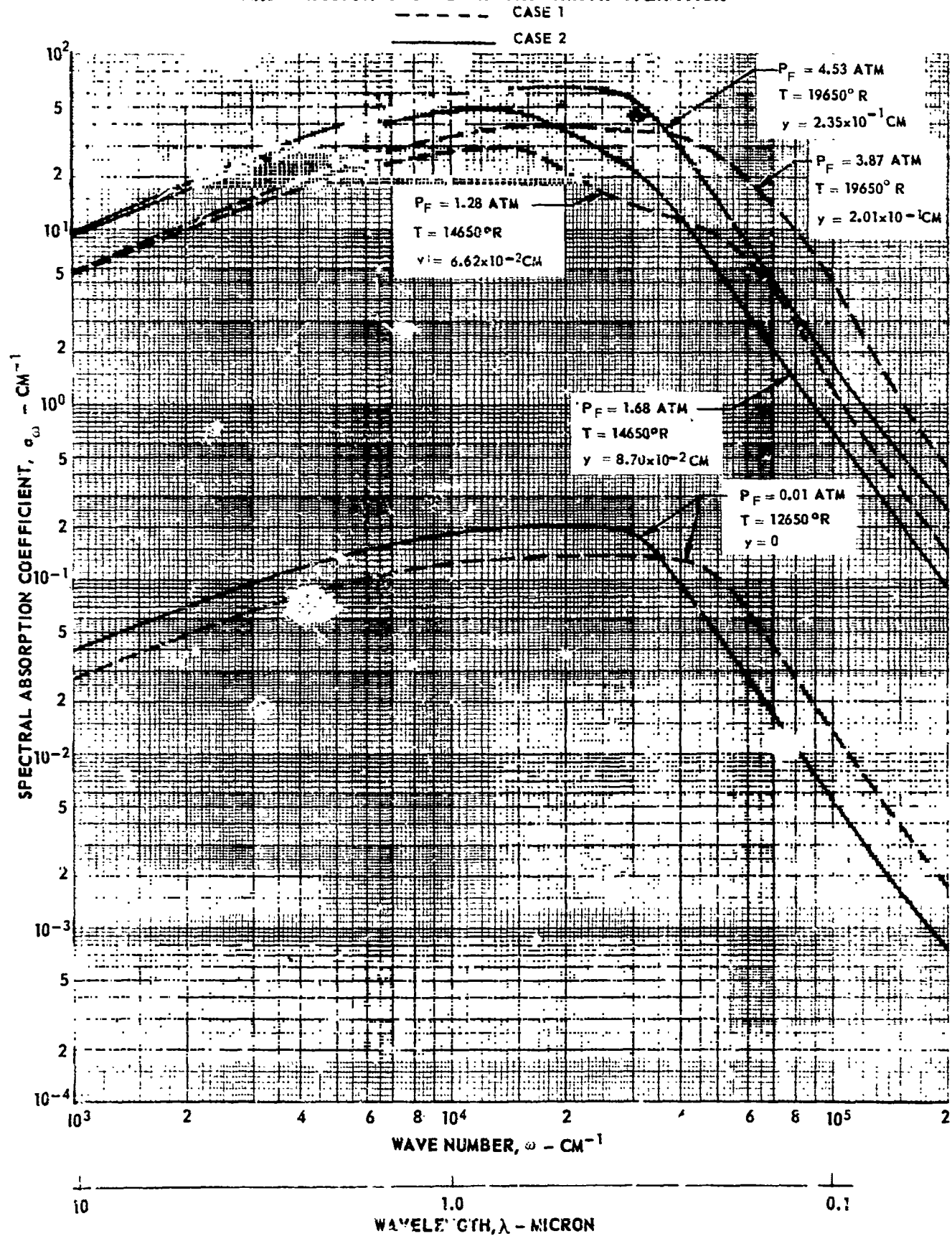


TEMPERATURE DISTRIBUTIONS IN FUEL REGION

FIG. 13

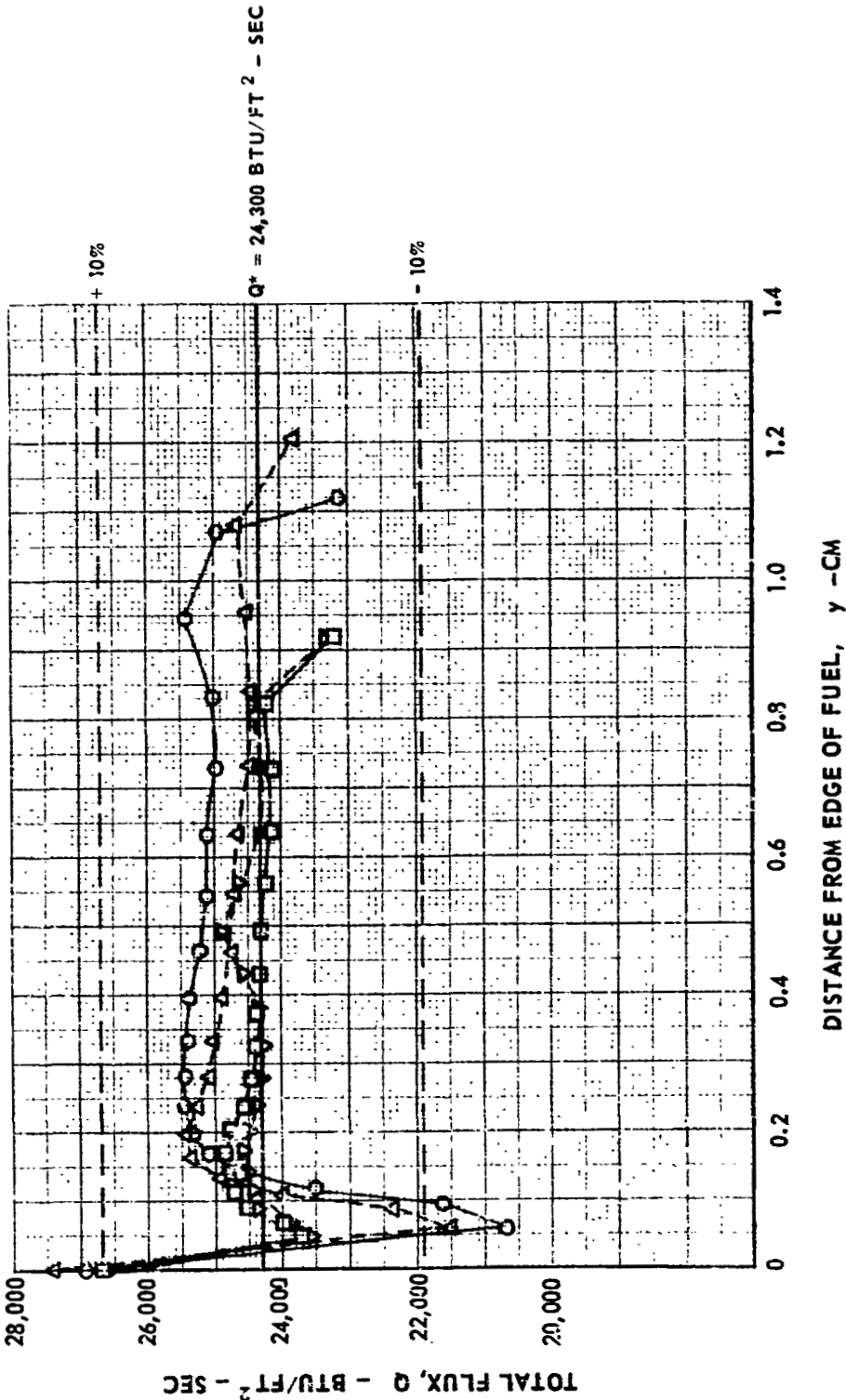


SPECTRAL ABSORPTION COEFFICIENTS OF NUCLEAR FUEL AT VARIOUS TEMPERATURES AND PRESSURES USED IN THE NINTH ITERATION

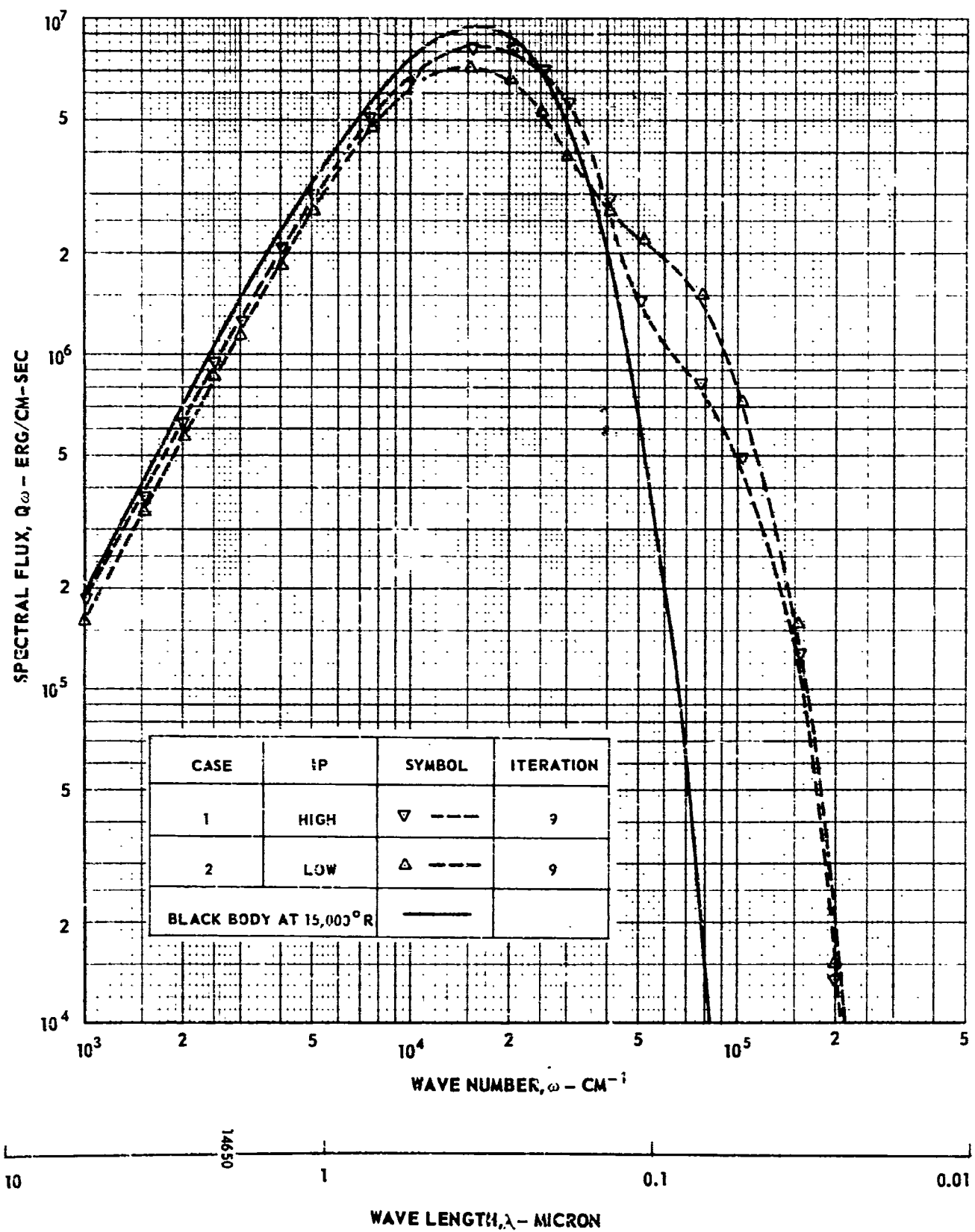


TOTAL FLUX DISTRIBUTION IN THE FUEL REGION

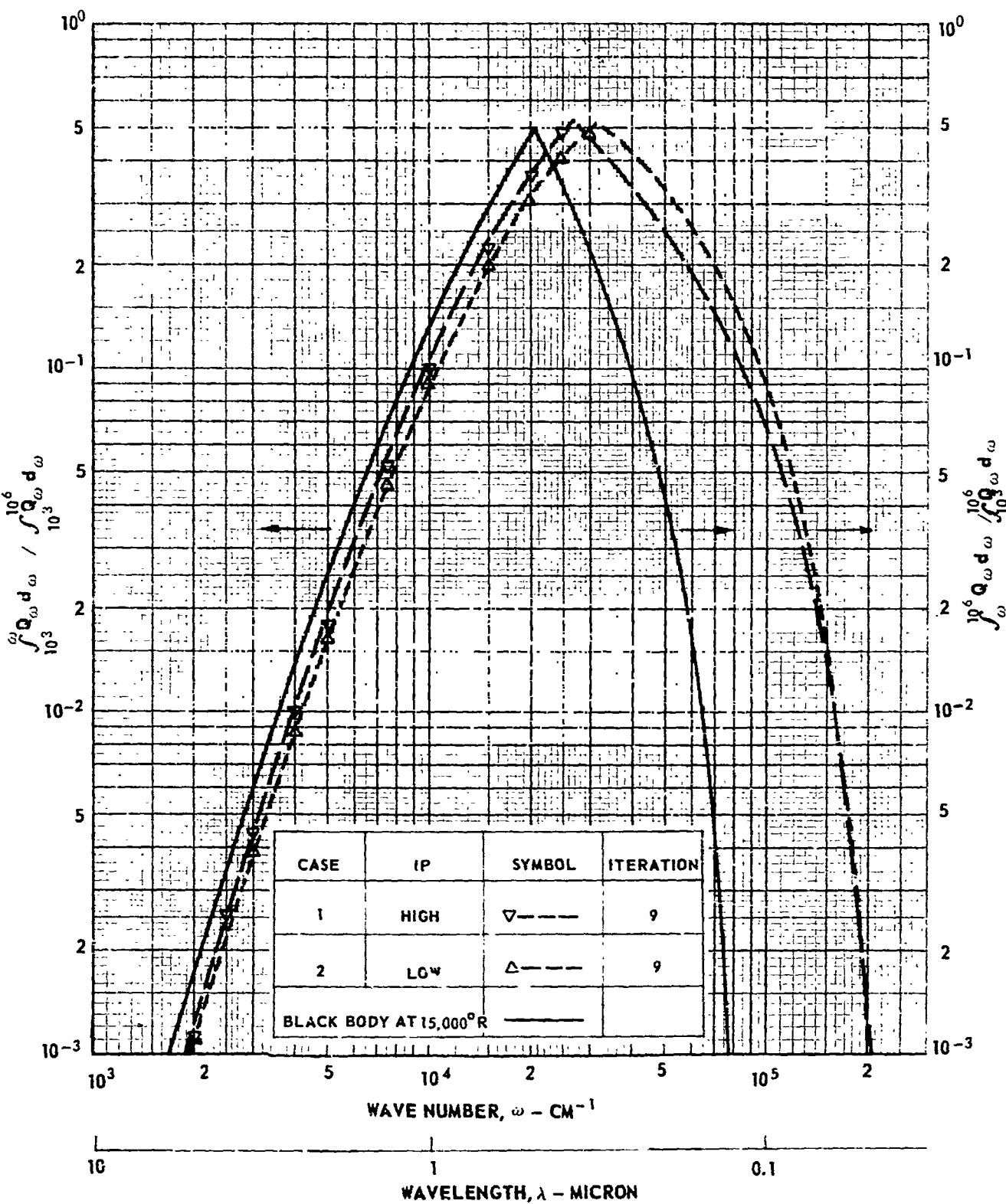
CASE	IP	SYMBOL	ITERATION
1	HIGH	□	8
		▽	9
2	LOW	○	8
		△	9



COMPARISON OF SPECTRAL FLUX AT EDGE OF FUEL AND 15000R BLACK BODY SPECTRUM



COMPARISON OF FRACTIONAL SPECTRAL FLUX DISTRIBUTION AT EDGE OF FUEL AND FRACTIONAL SPECTRAL FLUX DISTRIBUTION FOR A BLACK BODY 15,000 DEG R



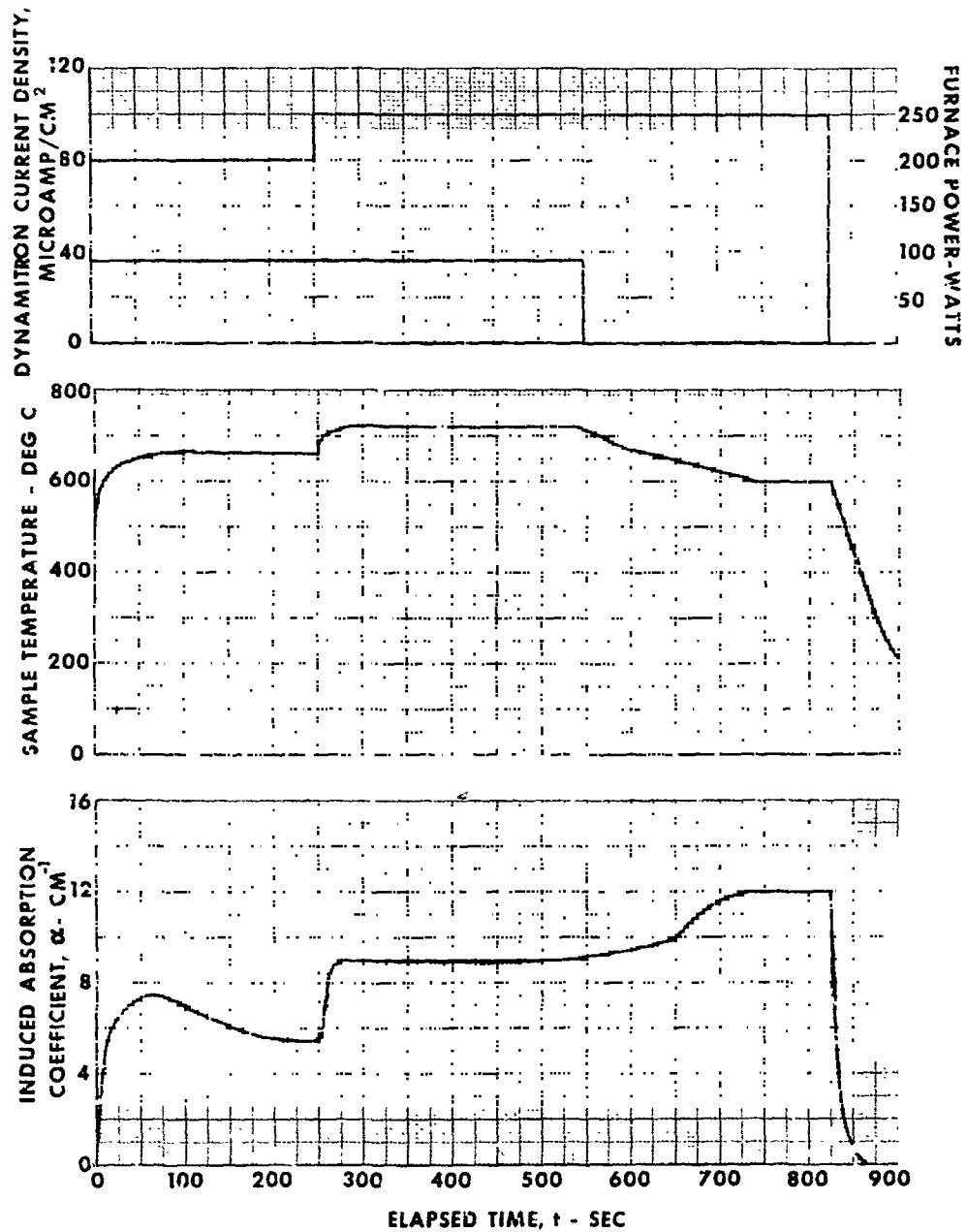
INDUCED ABSORPTION COEFFICIENT, CURRENT DENSITY AND SAMPLE TEMPERATURE DURING RUN 10

$$\lambda = 2150 \text{ \AA}$$

SPECIMEN NO. 1

PRE-IRRADIATION ROOM-TEMPERATURE ABSORPTION COEFFICIENT = 0.0

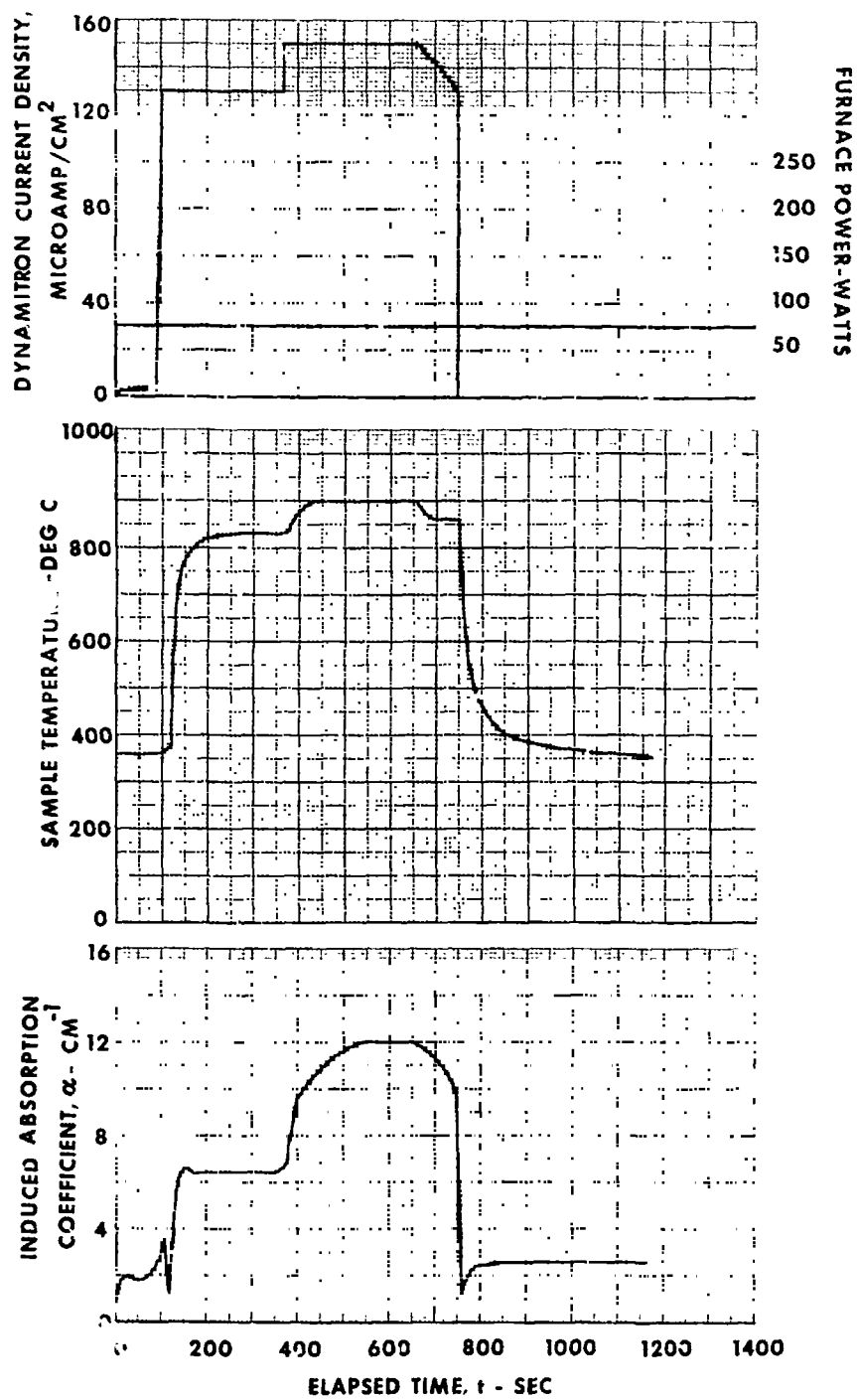
POST-IRRADIATION ROOM-TEMPERATURE ABSORPTION COEFFICIENT = 0.0



**INDUCED ABSORPTION COEFFICIENT, CURRENT DENSITY
AND SAMPLE TEMPERATURE DURING RUN 14** $\lambda = 2150 \text{ \AA}$

SPECIMEN NO. 2

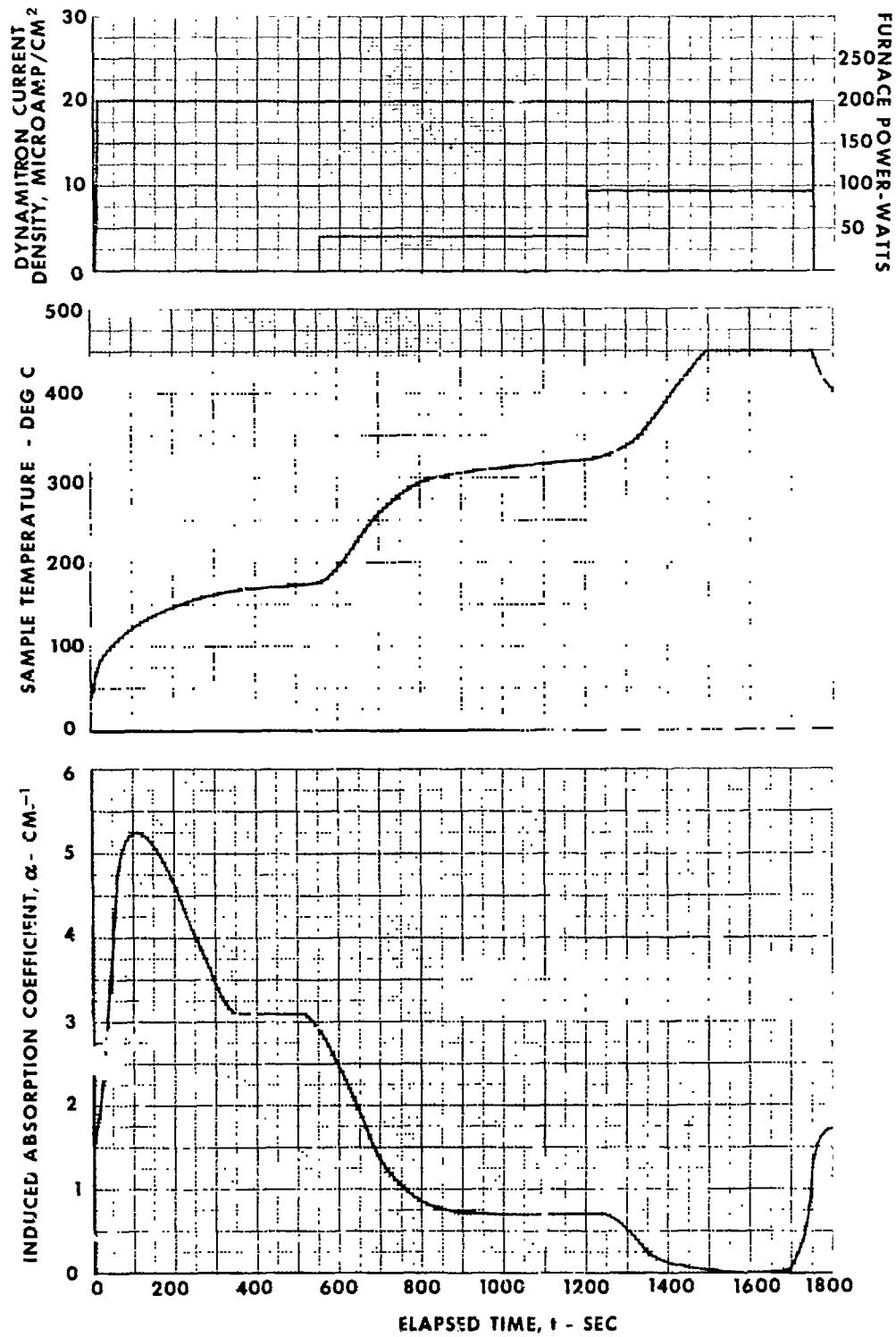
PRE-IRRADIATION ROOM-TEMPERATURE ABSORPTION COEFFICIENT = 0.0
POST-IRRADIATION ROOM-TEMPERATURE ABSORPTION COEFFICIENT = 2.1



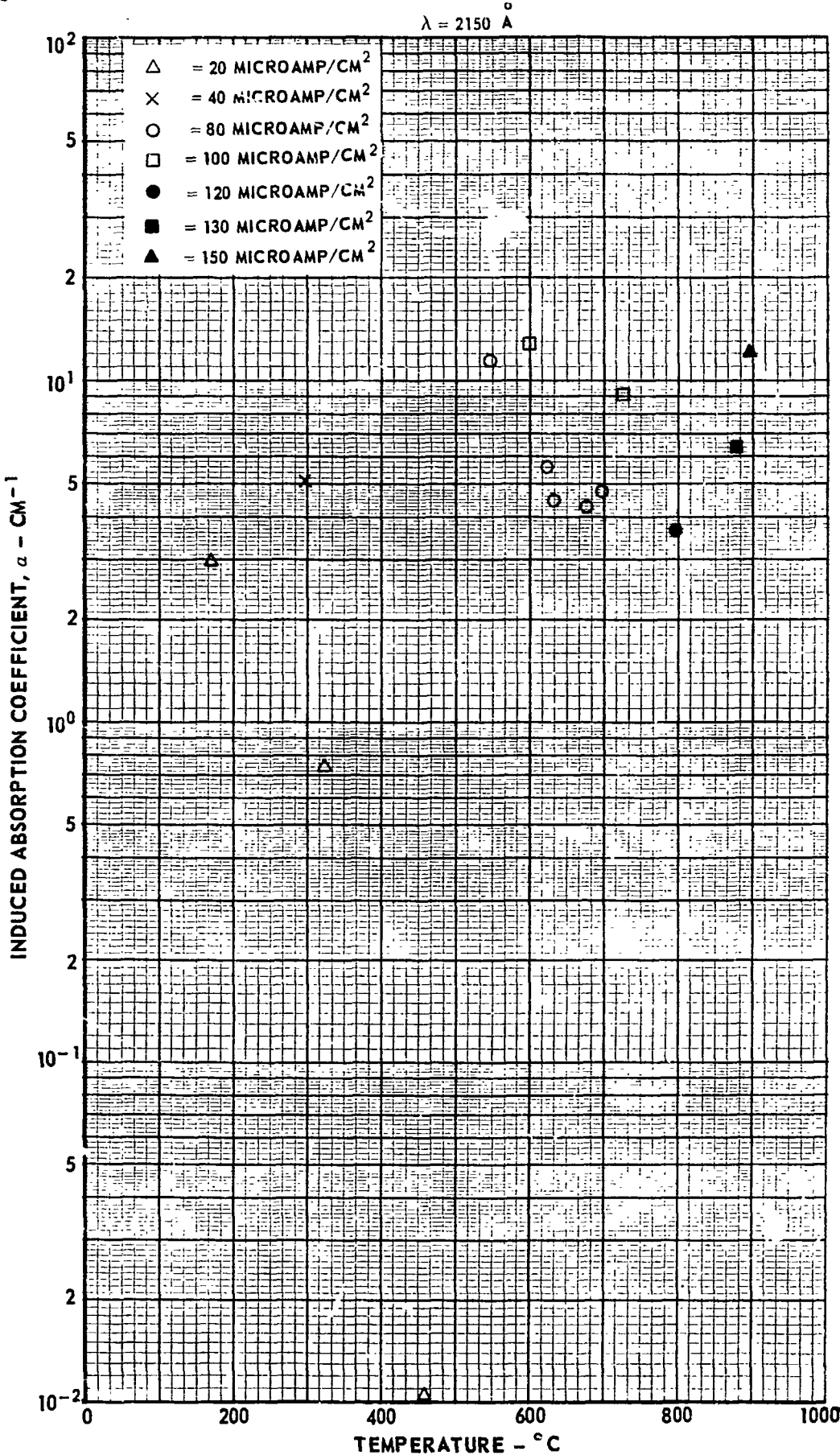
INDUCED ABSORPTION COEFFICIENT, CURRENT DENSITY
AND SAMPLE TEMPERATURE DURING RUN 15

$\lambda = 2150 \text{ \AA}$ SPECIMEN NO. 6

PRE-IRRADIATION ROOM-TEMPERATURE ABSORPTION COEFFICIENT = 1.55
POST-IRRADIATION ROOM-TEMPERATURE ABSORPTION COEFFICIENT = 1.57

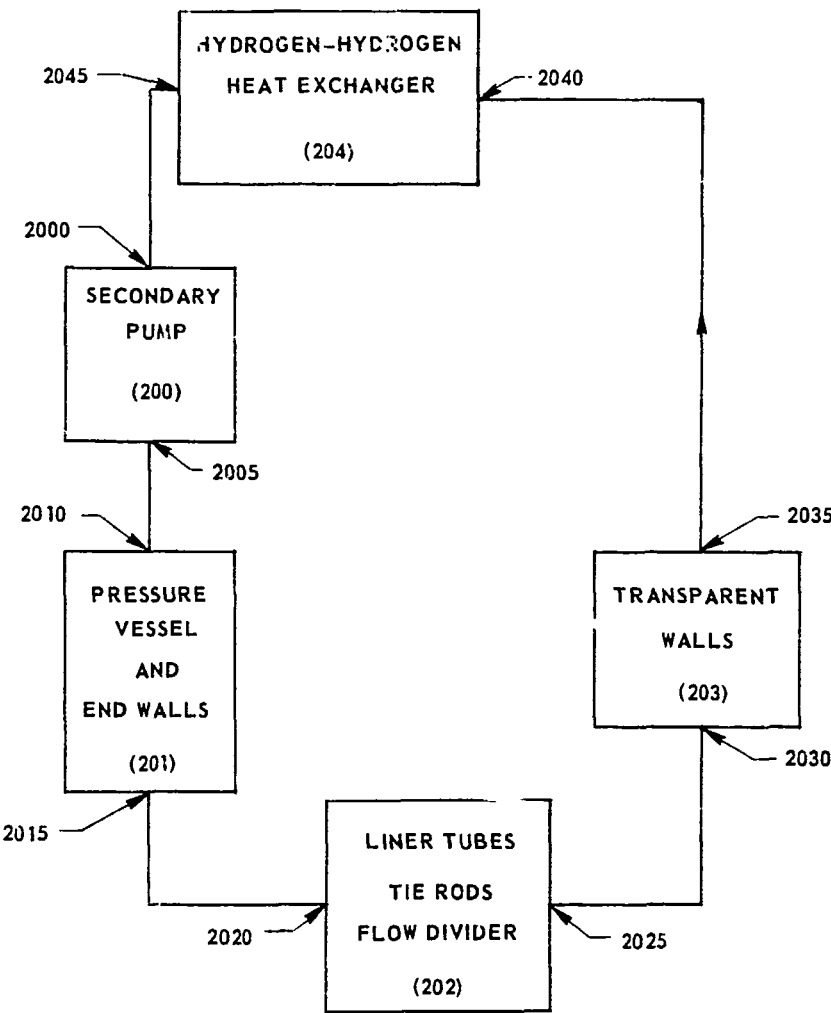


EQUILIBRIUM INDUCED ABSORPTION COEFFICIENT VS SAMPLE TEMPERATURE



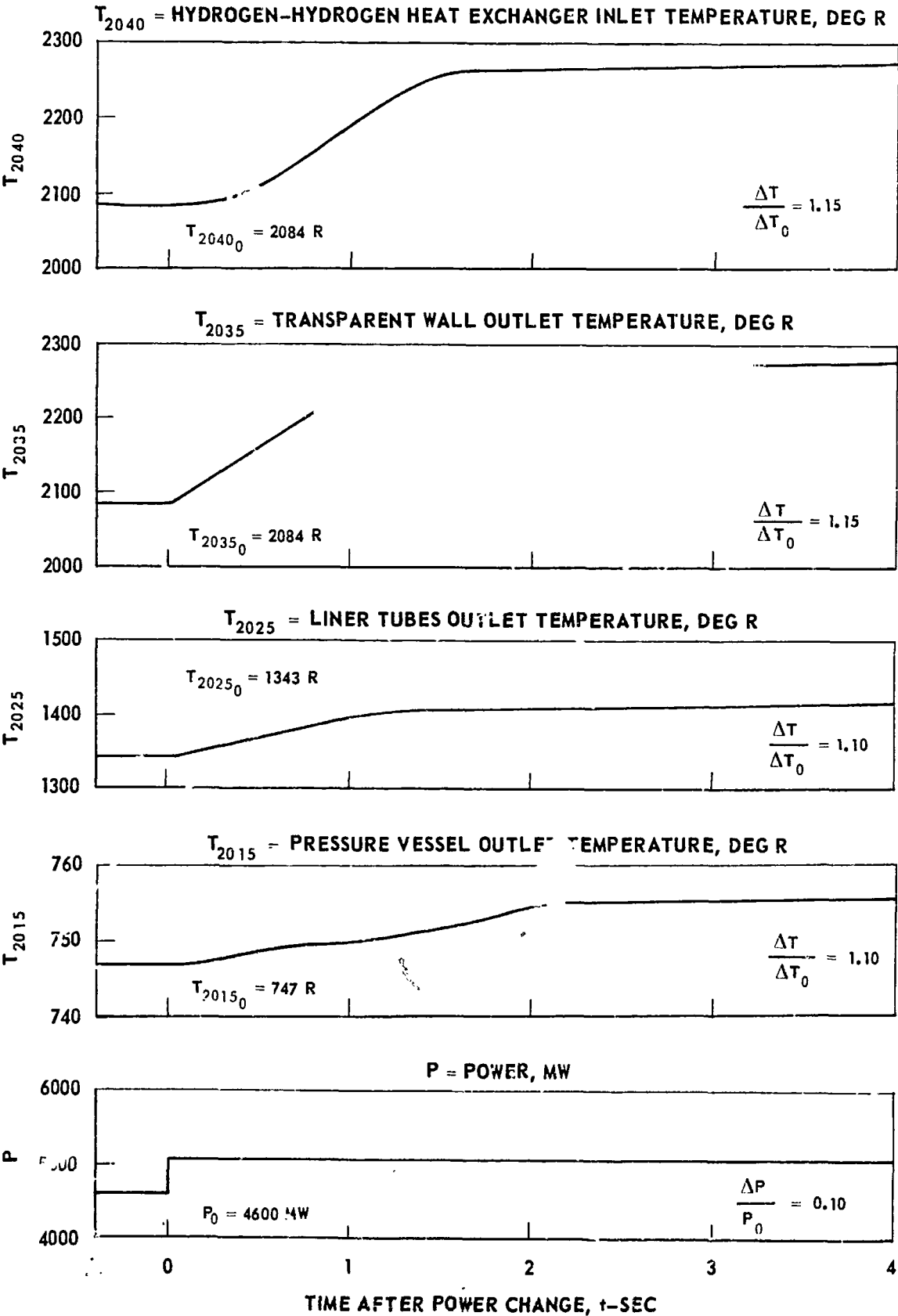
NUCLEAR LIGHT BULB SECONDARY COOLANT CIRCUIT

REGION NUMBERS ARE THREE DIGIT NUMBERS SHOWN IN PARENTHESIS
LOCATION NUMBERS ARE FOUR DIGIT NUMBERS



TEMPERATURE RESPONSES IN NUCLEAR LIGHT BULB SECONDARY COOLANT CIRCUIT
TO POSITIVE STEP CHANGE IN POWER

FOUR DIGIT SUBSCRIPTS DENOTE LOCATIONS SHOWN IN FIG. 22



TEMPERATURE RESPONSES IN NUCLEAR LIGHT BULB SECONDARY COOLANT CIRCUIT TO NEGATIVE STEP CHANGE IN POWER

FOUR DIGIT SUBSCRIPTS DENOTE LOCATIONS SHOWN IN FIG. 22

